6-8-2022 10:45 AM

Quantitative Image Analysis of White Matter Dysregulation Using Brain Normalization for Diagnostic Analysis of Pediatric Hydrocephalus

Renee-Marie Ragguett, *The University of Western Ontario*

Supervisor: de Ribaupierre, Sandrine, *The University of Western Ontario*
Co-Supervisor: Eagleson, Roy, *The University of Western Ontario*
A thesis submitted in partial fulfillment of the requirements for the Master of Engineering Science degree in Biomedical Engineering

Abstract

Surgical management for hydrocephalus is among the most common procedures performed by pediatric neurosurgeons. However, how to best predict postoperative outcomes is unknown. Neuroimaging studies could provide insight, though working with these images is non-trivial. This thesis aims to 1) evaluate registration and preprocessing methodologies to best prepare data for comparisons, and 2) assess the impact of postoperative lateral ventricle volume (LVV) as a predictor of white matter health in networks that are dysregulated in hydrocephalus patients. We found that skull-stripped, bias corrected images with the SyN algorithm produced most accurate registration. We also found large dysregulated white matter networks in patients, and postoperative LVV did not have a large impact in predicting these networks.

Overall, these studies suggest an image processing pipeline for pathological pediatric images and adds to the knowledge surrounding both the impact of pediatric hydrocephalus on white matter networks and the association with postoperative LVV.

Keywords

Pediatric Hydrocephalus, White Matter Integrity, Image Registration, Tractography, Ventricle Volume

Summary for Lay Audience

Hydrocephalus is a neurological disease that occurs in approximately 0.1% of births world-wide and is characterized by increased cerebrospinal fluid in the ventricles of the brain. Treatment for hydrocephalus involves redirecting the excess fluid from the ventricles to another part of the body, for example the peritoneum which is seen in the ventriculoperitoneal (VP) shunt. Despite being one of most common surgeries performed in children, there are many questions surrounding how to best predict postoperative outcomes. Utilizing neuroimaging techniques can allow us to better understand the disease. One challenge when working with neuroimages of children with hydrocephalus is that there can be difficulty when trying to compare these neuroimages with those of healthy children (e.g., normalization). This difficulty arises from morphological differences such as large ventricles, other pathologies in the brain, and treatment related non-correspondence (i.e., the VP shunt). In the first study, various different image preprocessing steps and normalization algorithms were assessed. It was found that images that were bias corrected as well as skull-stripped had better normalization accuracy relative to those that were not, and the best performing algorithm was SyN by Advanced Normalization Tools. In the case wherein these preprocessing steps are not possible, the DARTEL toolbox also performed with relatively high accuracy. In the second study, taking a whole-brain approach, white matter integrity and connectivity were compared between pediatric patients with hydrocephalus and healthy controls. Furthermore, postoperative ventricle volume was explored as a predictor for the white matter metrics in hydrocephalus patients. We found a series of large, dysregulated networks in patients with hydrocephalus relative to controls, many suggested decreased white matter integrity, and decreased white matter connections. Most networks involved subcortical structures and those outside the frontal lobes. After correction for multiple comparisons only white matter metrics in two streamlines were predicted by ventricle volume.

In summary, this thesis adds to the current knowledge of image processing pipelines for pathological pediatric images, and both the impact of pediatric hydrocephalus on white matter networks and the association with postoperative lateral ventricle volume.

Co-Authorship Statement

Co-Authorship Statement

This thesis contains material from two manuscripts, each its own chapter. The manuscripts are in preparation for publication. All work was completed under the supervision of Dr. Sandrine de Ribaupierre and Dr. Roy Eagleson.

Chapter 2:

R.M. Ragguett, R. A. Eagleson, S. de Ribaupierre (2022): "*Evaluating Registration and Preprocessing Methodologies for the Normalized Analysis of Brain MRI in Pediatric Patients with Shunt-Treated Hydrocephalus"* in preparation for the journal Human Brain Mapping.

My contribution to the study included the idea development, study design, methodology, data-analysis, data-interpretation, figure generation, and manuscript preparation. Dr. Sandrine de Ribaupierre, and Dr. Roy Eagleson, contributed to methodology, data-analysis, data-interpretation, as well as manuscript writing and revisions.

Chapter 3: R. A. Eagleson, S. de Ribaupierre (2022): "*Altered White Matter Networks, and Associations with Ventricle Volume in Children with Shunt Treated Hydrocephalus"* in preparation for the Journal of Neurosurgery: Pediatrics.

My contribution to the study included the idea development, study design, methodology, data-analysis, data-interpretation, figure generation, and manuscript preparation. Dr. Sandrine de Ribaupierre, and Dr. Roy Eagleson, contributed to methodology, data-analysis, data-interpretation, as well as manuscript writing and revisions.

Acknowledgments

First of all, I would like to thank my supervisors Dr. Sandrine de Ribaupierre and Dr. Roy Eagleson. Dr. de Ribaupierre, you have been a great role model for me. Your professionalism as a physician and scientist, combined with your unwavering work ethic is something I aspire towards. Dr. Eagleson, your determination and enthusiasm in the pursuit of information, is consistently a source of motivation. Together, your supervision, support, and guidance, were paramount in the completion of my thesis and all the opportunities throughout my Master's. I would also like to thank all my advisory committee members, Dr. Baron, Dr. Duerden, and Dr. Khan, for all your insight and feedback during my committee meetings. Thank you to all the Brain3DViz lab members for your support and comradery throughout my Master's. I'm very grateful to have been part of a lab with such diverse interests, demonstrating the complex problems that can be tackled with the power of collaboration. A special thanks to both Daiana Pur and Daamoon Ghahari for your encouragement and helping me get oriented to the data. Finally, I'd like to thank my friends and family for all their support over the years.

Table of Contents

List of Tables

List of Figures

List of Appendices

Chapter 1

1 Introduction

Hydrocephalus is a heterogeneous neurological disease characterized by an abnormally large volume of cerebrospinal fluid (CSF) in the ventricles of the brain as seen in Figure 1.

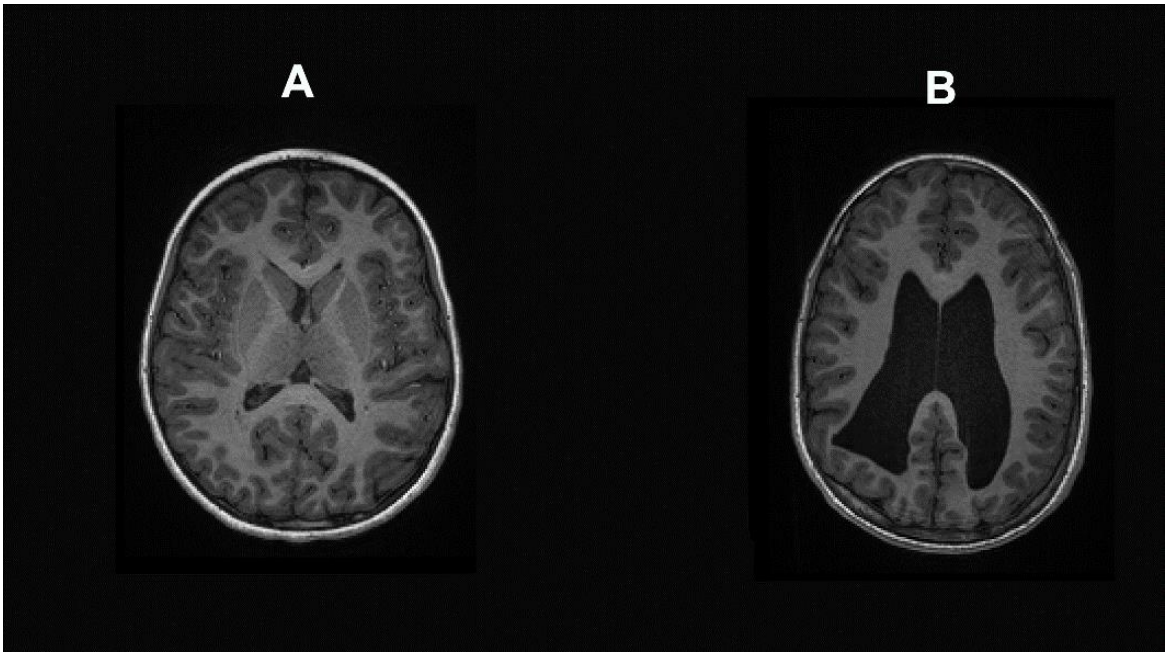

Figure 1: Structural MRI images where A is a healthy control and B is a patient with hydrocephalus. The cerebral ventricles are dark and centrally located in both images.

Occurring in approximately one in every 1000 births world-wide, with a higher incidence in low-income countries, treatment for pediatric hydrocephalus represents one of the most common procedures completed by pediatric neurosurgeons (Dewan et al., 2018). The impact pediatric hydrocephalus has on the healthcare system further underscores its importance. Specifically, in the United States, hydrocephalus related hospital admissions are responsible for a disproportionately large number of days spent in hospital (Simon et al., 2008). Despite the impact hydrocephalus has on the patient and the healthcare system, it remains an under-studied disease.

Various preclinical studies have demonstrated that enlarged ventricle size and increased intracranial pressure can impact the surrounding neuronal tissues through various processes. For example, studies have shown stretched white matter tracts, reduced myelin, and destroyed axons. Specifically, periventricular white matter appears to be most vulnerable, though some studies have reported distal effects (Del Bigio, 1993; Del Bigio et al., 2003; Tan et al., 2018). The ability to use diffusion imaging in patients with hydrocephalus allows researchers to characterize white matter integrity *in vivo*, by assessing the diffusion of water in the neurons. Using this technique applied to brains following surgical treatment, we may be able to better understand the impact of surgical treatment, and surgical decisions on postoperative white matter health.

Though there is interest in utilizing neuroimaging techniques in children with hydrocephalus, the ability to work with these neuroimages and compare them to normally developing children can be difficult due to non-typical features in these images (e.g., large ventricles, non-typical brain shape, other pathology, and artifacts from treatment. See Figure 2).

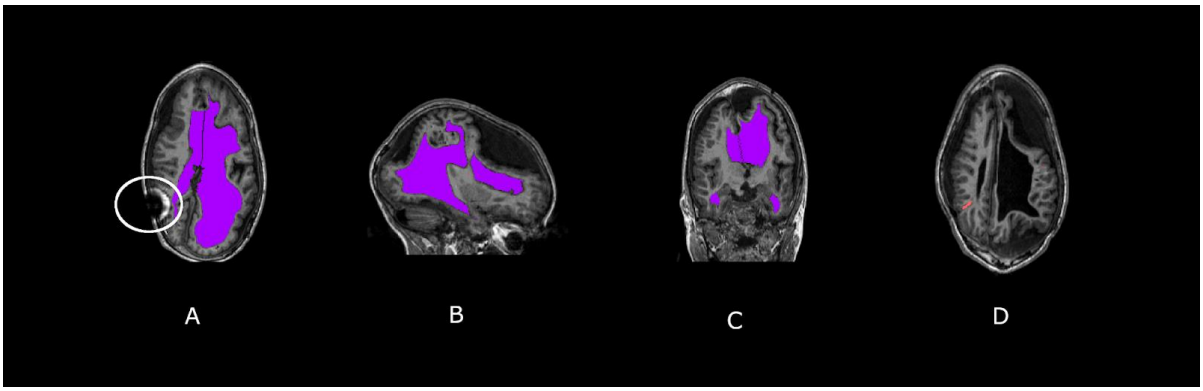

Figure 2: Characteristic brain asymmetries seen in pediatric hydrocephalus. A, B and C, have the ventricles segmented in purple and highlight the potentially non-typical brain shape. The circle in A outlines an artifact that can occur as a result of the shunt. D shows the catheter segmented in orange.

In some cases, this can result in the exclusion of participants with large ventricles from studies, in part due to the inability to accurately register their neuroimage to a standard space, therefore not allowing the comparison between participants (Tan et al., 2018). The systematic

exclusion of these participants and the inability to utilize this data has the potential to bias results and does not enable a full representation of the disease.

Pediatric hydrocephalus therefore provides an interesting pathology by which to explore both the impact of neuroimaging pipelines on the accuracy of neuroimage normalization and examine postoperative white matter integrity throughout the brain as it relates to postoperative ventricle size.

1.1 Hydrocephalus

1.1.1 Etiology

Hydrocephalus has been formally defined as “an active distension of the ventricular system of the brain resulting from inadequate passage of CSF from its point of production within the cerebral ventricles to its point of absorption into the systemic circulation” (Rekate, 2009). The cerebral ventricular system is a series of interconnected cavities, composed of two large lateral ventricles, and two smaller ventricles which are the third, and the fourth ventricle. These ventricles are the site of CSF production, and they also allow the CSF to flow to the points of absorption (view Figure 3 for a visualization of the cerebral ventricles).

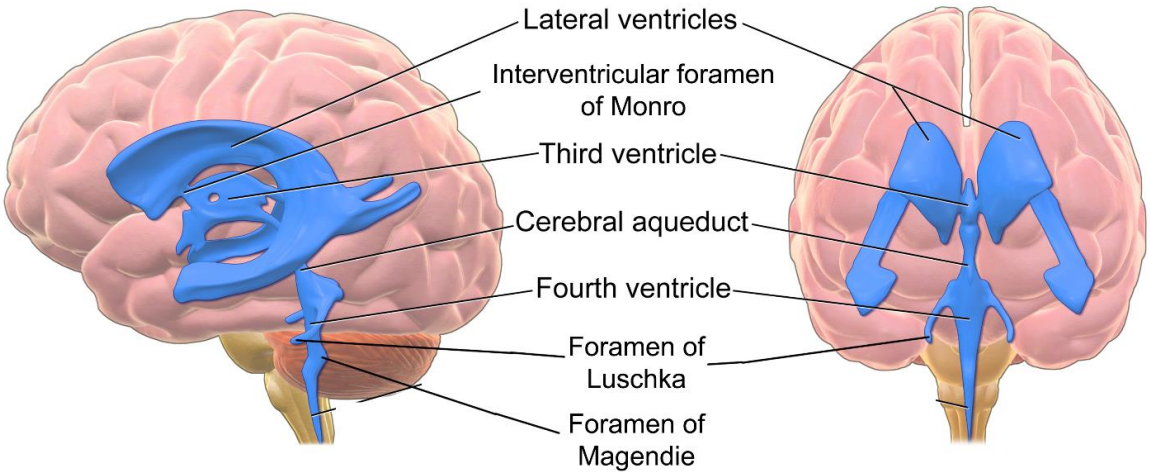

Figure 3: Labeled schematic of the cerebral ventricles.
Modified from Medical gallery of Blausen Medical, WikiJournal of Medicine, Wikiversity.

The CSF, which is a clear fluid, has various roles throughout the central nervous system including physical protection, waste removal, and the maintenance of homeostasis (Redzic et al., 2005; Spector et al., 2015). CSF is predominantly formed in the lateral ventricles by the choroid plexus, reaching the subarachnoid space and spinal canal by traveling through the ventricular system. Specifically, from the lateral ventricles, through the interventricular foramen of Monro, to the third ventricle. Then from the third to fourth ventricle through the cerebral aqueduct, and finally to the subarachnoid space and central canal through the foramen of Luschka and Magendie wherein it can be reabsorbed by the venous system through arachnoid granulations (Dandy, 1919).

The flow of the CSF through the aforementioned pathway is disrupted in hydrocephalus. There are many ways in which the flow of CSF can be disrupted, including an obstruction in the ventricular system, problems with reabsorption at the arachnoid granulations, or an overproduction of CSF (Ellington & Margolis, 1969; Rekate, 2008). Particularly premature babies that have hydrocephalus, the etiology is often bacterial meningitis or an intraventricular hemorrhage (Beni-Adani et al., 2006). Highlighting the varying etiology of hydrocephalus, there are many ways in which it can be classified (Oi, 2011). One such

classification is based on CSF dysregulation. Specifically, non-communicating or obstructive hydrocephalus, which is due to an obstruction in the circuit, as opposed to communicating hydrocephalus which is due to a problem with CSF flow after it exits the ventricular system. Another classification of hydrocephalus involves when the hydrocephalus was acquired. If it was present at birth, it can be termed developmental or intrinsic hydrocephalus. In contrast, if it was developed after birth with an obvious extrinsic cause, it can be classified as acquired or extrinsic hydrocephalus (Tully & Dobyns, 2014).

While there are many different ways to classify hydrocephalus, a final distinction to be made as it pertains to the current thesis is hydrocephalus diagnosed in childhood (infantile or pediatric hydrocephalus) in contrast to hydrocephalus diagnosed in adulthood. Hydrocephalus diagnosed during childhood is unique from that diagnosed in adulthood. One difference arises in the etiology, where with adult-onset hydrocephalus, hydrocephalus often develops secondary to other pathologies. Furthermore, common etiologies include tumors and vascular lesions (Bir et al., 2016). Additional differences may be seen due to the compensatory mechanisms postulated to occur alongside ventricle dilatation, which are in part explained by the Monro-Kellie hypothesis. The Monro-Kellie hypothesis postulates, there exists a constant volume in the skull which is composed of CSF, brain tissues (i.e., white and gray matter), and blood vessels. Further, if one component changes volume, the other component's volume must change in the opposite direction (Mokri, 2001). The expectations of the Monro-Kellie hypothesis are however complicated in pediatric hydrocephalus when compared to adult onset hydrocephalus, particularly in very young children wherein the cranial sutures are not yet fused. As a result the skull is able to expand to accommodate the increased ventricular volume, therefore the impact on the surrounding tissues can be different (Harold L Rekate, 2020). It follows, when the cranium can expand, the ventricles can expand much larger with a smaller elevation in intracranial pressure and while the axons still stretch, a cytotoxic hypoxic environment is less likely. Additionally, pediatric brains are still undergoing development. One area of interest is myelination, wherein major myelination increases occur over the first few years of life (Welker & Patton, 2012). Some studies have shown a negative correlation with myelination and ventricular dilation such that with decreased myelin, ventricles can dilate further (Hanlo et al., 1997). It is therefore not surprising that the etiology of pediatric hydrocephalus differs from adult

onset hydrocephalus, and even differs throughout pediatric hydrocephalus partially corresponding to when the cranial sutures begin to fuse, and neurodevelopmental milestones (Rizvi & Anjum, 2005).

1.1.2 Clinical Presentation

The clinical presentation and features of children with untreated hydrocephalus can vary based on age. Specifically, one of the main differences between infantile hydrocephalus wherein the children have hydrocephalus in the first two years of life, and hydrocephalus diagnosed after this time, is that the cranial sutures are not fused in the earlier case. This allows the cranium to expand, adjusting to the ventricle dilation. Indeed, the enlarged cranium is often one of the most evident signs of infantile hydrocephalus. Common clinical signs of hydrocephalus include changes in head shape, such as an enlarged cranium, or a bulging anterior fontanelle (Kirkpatrick et al., 1989). Other clinical features include splayed sutures, particularly prominent scalp veins, and “sunsetting” eyes wherein “sunsetting” occurs when there is a downward pressure on the eyes resulting in a persistent downward gaze (Boragina & Cohen, 2006). Other symptoms can include delayed growth and neurological development, increased muscle tone, increased headaches, and vomiting (Rizvi & Anjum, 2005).

1.1.3 Treatment

The goal for management of hydrocephalus is to reduce the volume of CSF in the cerebral ventricles thereby reducing the intracranial pressure. Hydrocephalus is most often treated surgically. Common surgical procedures for hydrocephalus include the endoscopic third ventriculostomy, wherein the floor of the third ventricle is penetrated allowing the CSF to flow to the basal cistern, or insertion of a shunt which diverts the CSF. The current thesis focuses on hydrocephalus which has been treated using a non-programmable VP shunt.

Shunting is one of the most frequent surgeries performed for the management of hydrocephalus. A shunt allows the excess fluid from the ventricles to be redirected into a different body cavity, such as the peritoneum (i.e., the ventriculoperitoneal [VP] shunt). Other less common configurations for shunts include the ventriculoatrial shunt and the lumboperitoneal shunt which drain from the ventricle to the atria and from the spine to the

peritoneum respectively. The VP shunt generally involves the insertion of a proximal catheter into one of the ventricles. This catheter is attached to a valve and a distal catheter, which is placed subcutaneously along the skull to the peritoneum allowing the extra CSF to drain and be absorbed (Pople, 2002). Notably, some shunt systems (e.g., adjustable valves) allow the physician to externally and non-invasively adjust the pressure needed to open the valve and drain the CSF. Thus, in cases wherein too much CSF is draining, and "slit-ventricle syndrome" has occurred, ventricle size could be increased in a non-invasive fashion using the adjustable valve. While shunting has been shown to alleviate some hydrocephalus symptomatology (e.g., reduced intracranial pressure), ultimately there are many outstanding questions surrounding the outcome of shunt surgery for hydrocephalus. Especially in young infants, there is no consensus on exact timing of treatment, particularly when temporary treatment is necessary, or how to best predict the cognitive outcome of treatment (Flannery et al., 2014; Paulsen et al., 2015).

Though it is an incredibly common treatment, the VP shunt surgery has a high rate of failure. Some of the most common complications that can arise alongside VP shunt surgery include infection, and shunt obstruction. Less common complications include abdominal pseudocyst, bowel perforation, and subdural hematoma (see Paff, et al., 2018 for a detailed review) (Paff et al., 2018). In cases wherein there are shunt complications, shunt revision surgery can be performed. This procedure is not uncommon, and many patients with VP shunt treated hydrocephalus are expected to undergo shunt revision surgery during their lifetime, some even requiring multiple revisions (Stone et al., 2013). Factors that positively contribute to the rate of shunt revisions include low socioeconomic status, obstructive hydrocephalus, and being younger than 19 years of age (Wu et al., 2007).

1.1.4 Treatment Outcomes

When assessing the outcome of surgery for hydrocephalus, there are many possible metrics that can be assessed (e.g., cognitive, neurological, or neurodevelopmental deficits). The outcomes of surgery for hydrocephalus have been previously classified, in brief, as: surgical outcomes (e.g., rate of shunt infection or malfunction), mortality (e.g., related to the shunt device, or others causes), morbidity (e.g., cognitive, motor, headaches, and endocrine), and functional/social (e.g., schooling, and social integration) (Vinchon et al., 2012). Of these

categories, neuronal structure could have an impact on various morbidity and functional/social outcomes. For example, some studies have found that volumetric measurements of white and gray matter in patients with pediatric hydrocephalus corresponded to various cognitive functions (Fletcher et al., 1996). Given these associations, identifying methods to predict and characterize neuronal changes following VP shunt surgery for pediatric hydrocephalus may be beneficial.

1.1.4.1 Impact on White Matter

Untreated hydrocephalus is associated with a range of potential pathological changes to white matter such as stretching, and demyelination (Del Bigio, 1993). Preclinical studies have demonstrated that neurons that were damaged prior to treatment can experience some recovery; however the extent of recovery depends on their proximity to the ventricles. Neuronal recovery following shunt insertion is greater when the tissues are further away from the ventricles (Aoyama et al., 2006; da Silva et al., 1995). Some clinical studies have further demonstrated that white matter differences exist between healthy controls and patients with treated hydrocephalus. For the most part, white matter integrity is often worse in patients with hydrocephalus relative to controls (Hasan et al., 2008; Koyama et al., 2013; Rajagopal et al., 2013). Furthermore, while there is no way to best predict white matter integrity following surgery, some studies have suggested that postoperative lateral ventricle volume is a positive predictor of white matter integrity and associated with improved outcomes (Tan et al., 2018; Williams et al., 2015).

1.1.4.2 Postoperative ventricle volume

Following shunting surgery the cerebral ventricles can vary in size until reaching their final size at approximately 14 months post operation. Ventricle size in pediatric hydrocephalus can be impacted by a variety of factors including patient specific factors such as initial ventricle size, growth of brain tissues, and growth of the cranium (Tuli et al., 1999). In addition to patient specific factors, surgical decisions and shunt implementation can also impact the final ventricle size. For example, as the valves on the shunt function using principles of pressure, there are complications which arise which can result in unfavorable fluid dynamics. Specifically, “slit-ventricle syndrome” (i.e., chronic over drained ventricles) can arise in

some cases due to the patient standing upright (Hanak et al., 2017). Given the variability in postoperative ventricle size, it has been studied in the literature as it relates to various postoperative outcomes. In short, a systematic review conducted by Nikas, et al., (2014) determined that postoperative ventricle volume as measured by the frontal and occipital horn ratio does not have sufficient evidence in the literature to be a predictor of efficacy of treatment. Notably, there are various different methods to approximate ventricle volume, and while the frontal and occipital horn ratio is highly correlated with ventricle volume, it is not as precise as volumetric ventricle volume which can be achieved through segmenting the cerebral ventricles (O'Hayon et al., 1998; Radhakrishnan et al., 2019). Using volumetric measurements, some studies have investigated postoperative ventricle volume as a predictor for white matter integrity and some of the studies have found that larger ventricles were indicative of white matter resembling healthy controls (i.e., increased fractional anisotropy (FA) – suggesting increased white matter integrity), and related to better outcomes (e.g., reduced headaches), although other reports conflict with this (Kulkarni et al., 2015; Tan et al., 2018; Williams et al., 2015). None of these studies have investigated the association of postoperative ventricle volume with whole brain structural connectivity, or included region to region streamline counts, which ultimately may help to provide additional information about white matter organization wherein the varying image processing techniques are discussed in the following section (Section 1.3 Diffusion-Weighted Magnetic Resonance Imaging [MRI]).

1.2 Brain Imaging Normalization

When performing neuroimaging studies, a common goal is to compare differences between groups or across various studies. For example comparisons can be done using functional activation, structural connectivity, or changes in any of the aforementioned over time. To facilitate these comparisons, images must be in some common stereotaxic space. Some of the most frequently used common spaces in neuroimaging is the Montreal Neurological Institute (MNI) space, and the Talairach space (Evans et al., 1993; Talairach, 1988). When all neuroimages are in a common space, we’re able to compare one point and or structure between all images.

To ensure that all images are in a standard space, they have to be spatially normalized to a specific space such as the MNI space, using image registration. Registration, in short, is an

imaging technique that can be used to align one image to another image. When normalizing, each participant's three dimensional neuroimage is registered to a standard template, such as the MNI 152 template, which is an average image of a series of adult brains (Mazziotta et al., 2001; Mazziotta et al., 1995). Following this process, the original image is now normalized to MNI space.

Image registration is a non-trivial task, and various image registration algorithms exist allowing different transformations. In brief, registration algorithms are often divided into linear and non-linear or deformable registration. Linear registration can transform images by translation, rotations, sheers, or zooms (as depicted in Figure 4).

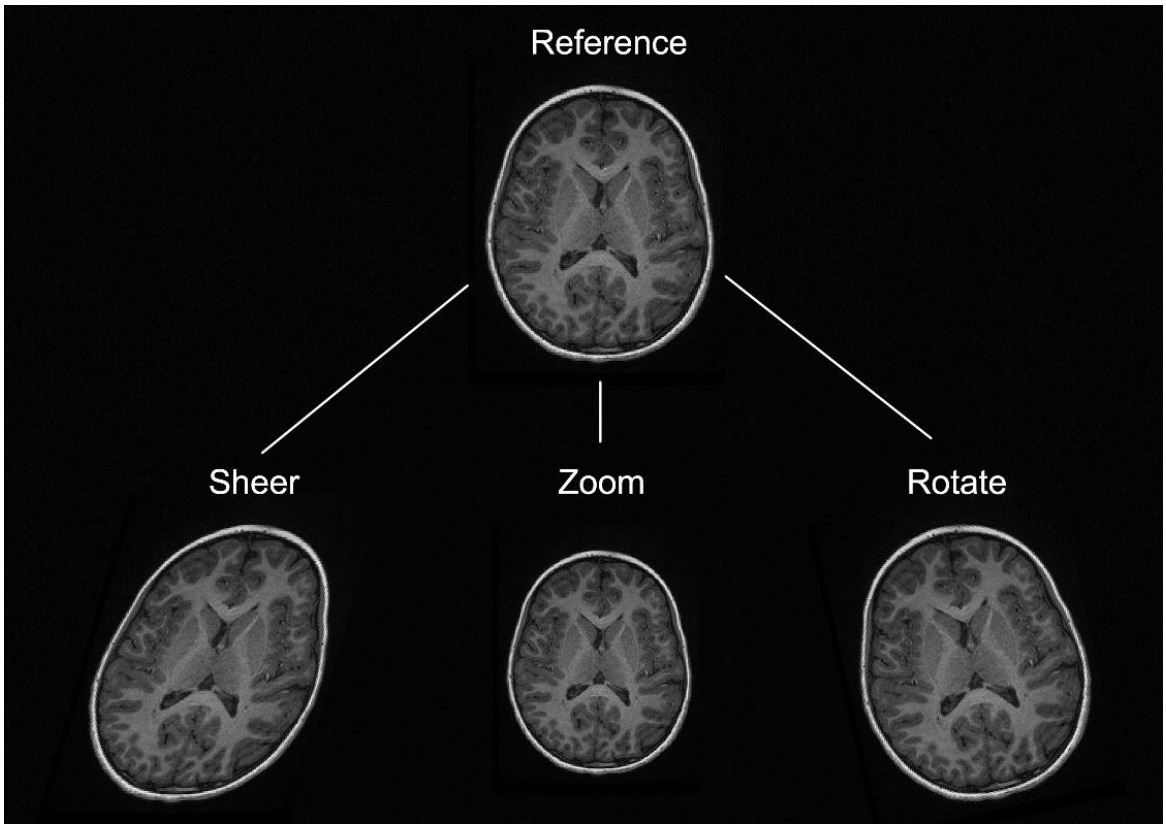

Figure 4: Various linear transformations applied to an MRI neuroimage.

In contrast, deformable registrations allow non-linear transformations and localized deformations. When registering a participant's neuroimage to the MNI template image, a combination of both linear and non-linear transformations are often used. Furthermore, there are various implementations of registration algorithms which may impact performance,

wherein differences can occur for example in the degrees of freedom, and similarity metrics (Hellier et al., 2003; Klein et al., 2009).

1.2.1 Implications of Poor Registration

If a registration is poor, there could be complete non-correspondence between structures making data unusable. It is not uncommon to find neuroimaging studies wherein participants have been excluded due to poor registration (Clarençon et al., 2017; Pannek et al., 2020; Tan et al., 2018). It has been suggested that misalignment in functional MRI can result in false negatives, or false positives driven by anatomical differences as opposed to differences in brain activity (Crinion et al., 2007). Indeed, recognizing the limitations of registration, there have been techniques developed that try to overcome these problems. For example one such technique found in DTI is tract-based spatial statistics (TBSS), where a maximum FA value is projected onto a white matter tract skeleton, reducing the need for a perfect registration (Smith et al., 2006). There are however limitations with TBSS surrounding anatomical specificity since the dimensionality of the white matter tracts are reduced (Bach et al., 2014). Taken together, accurate registrations are an important part of neuroimaging studies and despite attempts to reduce the need for incredibly accurate registrations, these methods still have limitations.

1.2.2 Challenges with Registration

There are many potential challenges to having accurate neuroimaging registrations. Ou, et al., (2014) have characterized some common complications into 4 different categories: 1) inter-subject anatomical variability, 2) intensity inhomogeneity, 3) protocol and field of view differences, and 4) pathology induced missing correspondence (Ou et al., 2014). It is not uncommon to find many of these challenges concurrently. For example, when working with pathological neuroimages in a pediatric population. Pediatric brains have anatomical variations due to age related differences wherein over time, there are changes in total brain volume, and volumes of gray matter and white matter tissues (Giedd & Rapoport, 2010; Jernigan & Tallal, 1990). There can also be non-correspondence introduced from pathology or treatment. For example a hemorrhage or a shunt could appear in a pathological image and would not appear in the template image.

1.3 Diffusion-Weighted MRI

Diffusion-weighted MRI is an imaging technique that can be used to estimate the underlying white matter connectivity of the brain, and investigate microstructural differences *in vivo*. Diffusion-weighted imaging makes use of the movement of water molecules, their random motion, and diffusion process (i.e., Brownian motion) to probe the white matter microstructure. As water does not easily pass through axonal cell membranes, the diffusion of the water is anisotropic, expected to travel along the direction of the axons. In contrast, when there is white matter damage, and for example increased demyelination, decreased number of axons, or damaged axons, you could expect reduced anisotropic diffusion (Horsfield & Jones, 2002).

There are various metrics that can describe white matter microstructure that are derived from diffusion-weighted MRI using the diffusion tensor model (i.e., diffusion tensor imaging [DTI]). The diffusion tensor model represents the direction of diffusion over three different directions describing an ellipsoid with three eigenvalues λ_1, λ_2, and λ_3 representing the magnitude of diffusion and three eigenvectors ε_1, ε_2, ε_3, representing the directions of diffusion. When all eigenvalues are equal, diffusion is considered isotropic in contrast, when the eigenvalues are unequal, we expect anisotropic diffusion. Using these values, diffusion within the white matter can be summarized and inferences can be made about white matter integrity.

There are a series of common measures of white matter microstructure that are frequently included in the literature. Most commonly, FA, which is a normalized measure used to describe the fraction of anisotropic diffusion of water, ranging from 0 (high isotropy) to 1 (high anisotropy). FA is commonly described as a measure of white matter integrity; however there are many features of white matter organization that can impact FA values (e.g., axonal packing, myelination, and axonal degeneration). Often other diffusion metrics are included to get a more complete picture of the white matter microstructure as not all metrics are sensitive to the same underlying white matter structure). For example, mean diffusivity (MD) which represents the average diffusion over all three directions. There is also axial diffusivity (AD) and radial diffusivity (RD) which represent the diffusion along the

long axis (i.e., the principal eigenvector) and perpendicular to the long axis respectively (Feldman et al., 2010).

Diffusion weighted imaging also allows for the reconstruction of white matter tracts throughout the brain using probabilistic diffusion tractography. Using diffusion tractography, insight can be gleaned into brain connectivity differences between groups. This approach has been taken in hydrocephalus wherein the structural connectome was characterized using graph analysis and it was revealed that white matter networks in children with hydrocephalus are dysregulated relative to healthy controls (Yuan et al., 2015). One limitation of tractography is traditionally, the streamline counts are not quantitative as the number of reconstructed fibers are not guaranteed to be synonymous with the underlying fibers. Recently, however, many implementations of tractography have started to address this limitation, allowing quantitative comparisons of streamline counts by adding a weight or multiplier to the streamlines to better estimate the connection density (Smith et al., 2015; Zhang et al., 2022).

1.4 Thesis Outline

Despite the surgical management of hydrocephalus being one of the most common surgeries completed by pediatric neurosurgeons, the disease remains understudied. While there are many neuroimaging approaches that can be taken to further understand functional or structural differences in hydrocephalus, they predominately all depend on being able to accurately and effectively work with these neuroimages in a common space. The objective of this thesis is to therefore, in Chapter 2, determine the efficacy of preprocessing steps and evaluate which freely available registration program produces the most accurate normalization. Furthermore, using the insight gained from Chapter 2, in Chapter 3, the impact of postoperative ventricle volume on whole brain structural connectivity is assessed using a variety of white matter metrics derived from diffusion weighted imaging.

1.4.1 Evaluating Registration and Preprocessing Methodologies for the Normalized Analysis of Brain MRI in Pediatric Patients with Shunt-Treated Hydrocephalus

Registration to a standardized template (i.e.“normalization”) is a critical step when performing neuroimaging studies. Pediatric patients with shunt treated hydrocephalus, represent an interesting area of study for evaluation of general-purpose registration algorithms. These images, in particular, present a number of intersecting challenges for registration, including potentially large deformations to both brain structures and overall brain shape, artifacts from shuts, and morphological differences corresponding to age. In this study, the efficacy of various available registration programs and preprocessing steps are assessed by performing over 590 registrations. Specifically, the preprocessing steps of skull-stripping and bias correction are considered, and five different algorithms that are freely available, are used to normalize the T1 MRI brain images of a group of pediatric patients with VP shunt treated hydrocephalus. The Dice Coefficient (DICE) and Hausdorff Distance (HD) are used to evaluate the registration of a series of cortical and subcortical structures. The accuracy of the registrations are also reported by individual participants according to lateral ventricle volume for two of the better performing algorithms.

The results of this study suggest that increased registration accuracy is achieved using both skull-stripped and bias corrected images and a diffeomorphic registration algorithm, specifically SyN by Advanced Normalization Tools (ANTs). Given that skull-stripping (i.e., segmenting the brain tissues from non-brain tissues) is a non-trivial task, we have also demonstrated that the DARTEL Toolbox also has high accuracy without any additional preprocessing steps. Overall, these results provide insight to the performance of registration programs that can be used for normalization of brains with complex pathologies.

1.4.2 Altered White Matter Networks, and Associations with Ventricle Volume in Children with Shunt Treated Hydrocephalus

There exists no best predictor for determining the success of surgical management for pediatric hydrocephalus. Though conflicted, some suggest that postoperative lateral ventricle volume may be a good predictor of postoperative white matter integrity. In this study, a whole-brain approach is taken with probabilistic tractography in combination with white

matter microstructure metrics to explore differences in white matter networks between shunt-treated pediatric hydrocephalus patients and healthy controls. When there were dysregulated networks, the relationship between these white matter networks and post-operative ventricle volume were further assessed.

This cross-sectional study in pediatric patients with hydrocephalus and healthy controls revealed using whole-brain probabilistic tractography that there are various networks with dysregulated white matter integrity. These dysregulated networks have tracts connecting structures all throughout the brain, though the regions are predominately located outside the frontal cortex. Post-operative ventricle volume did not predict the white matter integrity of many tracts following correction for multiple comparisons.

Chapter 2

2 Evaluating Registration and Preprocessing Methodologies for the Normalized Analysis of Brain MRI in Pediatric Patients with Shunt-Treated Hydrocephalus

2.1 Introduction

Pediatric hydrocephalus is a complex neurological disease characterized by an abnormally high volume of CSF in the cerebral ventricles. While there is interest in studying pediatric hydrocephalus using neuroimaging techniques to learn more about the disease, working with these images may prove to be difficult given the potentially large pathology induced deformations and artifacts from surgical treatment (e.g., shunts) (Ou et al., 2014; Patel et al., 2017). When performing neuroimaging studies, a common goal is to be able to compare findings between participants. In order to accomplish this, the neuroimages must be registered to a standard stereotaxic space (i.e., spatial normalization) such as the MNI space using a template image (e.g., MNI-152), such that there is a one-to-one correspondence between images (Mazziotta et al., 1995). Poor normalizations, wherein there is suboptimal alignment of brain regions relative to the template image, can have a variety of impacts on the results of neuroimaging studies. For example, in functional magnetic resonance imaging studies, poor normalizations can result in decreased sensitivity and false negatives wherein observed effects could be driven by structural rather than functional differences (Crinion et al., 2007). Therefore, it is not surprising that image registration is a non-trivial task, and there has been ongoing interest in assessing the accuracy of various programs used for registration (Crinion et al., 2007; Klein et al., 2009; Ou et al., 2014).

Image registration can be characterized by the possible transformation into two categories: linear and nonlinear. Linear registration in 3D can perform translations, rotations, scales, and skews in three directions (x, y, and z). In contrast, non-linear registration allows for deformations. Normalization can take advantage of a combination of both methods wherein there can be an initial linear registration followed by a non-linear registration. A number of freely available neuroimaging and medical imaging programs include functions for performing both these registrations (e.g., FMRIB Software Library [FSL,

https://fsl.fmrib.ox.ac.uk/fsl], and Statistical Parametric Mapping [SPM, https://www.fil.ion.ucl.ac.uk/spm]) (Ashburner, 2007; Smith et al., 2004).

Difficulty in performing registrations can occur for a variety of reasons. Ou et al., (2014), have operationalized the potential difficulties into four overarching challenges, which include: inter-participant anatomical variation, intensity and noise differences, protocol and field-of-view differences, and pathology induced missing correspondence. Often, there can be many of these challenges present in one dataset. For example, many of these challenges can be observed particularly in clinical pediatric populations wherein there can be pathology induced missing correspondence in addition to age-based anatomical variation (Courchesne et al., 2000).

There exist various methods to improve normalization accuracy with pathological brains. Tang, Wu, and Fan (2017) have characterized these methods into three overarching categories which include: masking, pathology simulation, and inpainting (Tang et al., 2017). Specifically, cost function masking, wherein a region of non-correspondence in the image is masked, has been shown to result in more accurate registrations (Brett et al., 2001). The generation of masks however can be incredibly time consuming, particularly in cases wherein the regions of interest cannot be accurately segmented automatically and there are many participants. Further, even when segmentation can be completed automatically, many segmentation methods are computationally intensive. As a result, there is interest in general purpose normalization pipelines which can be utilized for pathological images that can produce accurate results by tuning of parameters rather than extensive manual work and computationally expensive processes. This is particularly pertinent as the data associated with medical images are becoming increasingly large (Scholl et al., 2011).

To date, there have been no studies assessing the efficacy of various normalization pipelines for pediatric hydrocephalus. The normalization of neuroimages in those with shunt-treated pediatric hydrocephalus provides a unique series to study as these images represent a variety of challenges including non-correspondence and artifacts from shunt treatment, potentially large pathology induced deformities in the ventricles and surrounding tissues, and age-based anatomical variation. Indeed, once treated with a VP shunt, the ventricles can range from being smaller than normal, to staying extremely large depending on when the shunt is

inserted in the life of the child, and what type of valve is used. The objective of the current study is to assess the accuracy of a variety of freely available registration programs after preprocessing steps including image normalization in a population who has a wide variation of brain imaging.

2.2 Methods

2.2.1 Participants

Clinically stable children with hydrocephalus treated by VP shunts were recruited from a pediatric neurosurgical outpatient clinic in London, Ontario, Canada. Approval was obtained from our institutional research ethics board. Inclusion criteria included patients with hydrocephalus within the first two years of life or intraventricular hemorrhage at birth. Patients were not eligible for the study if they had a programmable shunt or any other contraindications for MRI. Figure 2 shows characteristics of neuroimages of those with pediatric hydrocephalus that could impact normalization.

2.2.2 Magnetic Resonance Imaging Acquisition

Neuroimages were acquired from a Siemens MAGNETOM Prisma 3-Tesla MRI scanner with a 32-channel head coil. A whole brain T1-weighted image was acquired using the three-dimensional magnetization-prepared rapid gradient-echo (MPRAGE) sequence (Repetition time [TR] = 2300ms ; Echo time [TE] = 2.93ms; Inversion time [TI] = 900ms; Flip Angle = 9° ; Matrix Size = 256 x 256, Number of Slices = 160; Field of View [FOV] = 256mm ; Resolution = 1.0 x 1.0 x 1.0 mm^3).

2.2.3 Image Preprocessing

Given the potential impact of image preprocessing on registration accuracy, various preprocessing steps were performed. Registrations were performed with and without skull-stripping, and with or without bias correction. Registration using the DARTEL Toolbox was performed only with whole-brain data as segmentation of the tissue types is required to run DARTEL and SPM’s segmentation tool will remove the non-brain tissues.

2.2.3.1 Skull-Stripping

Removal of non-brain tissues was completed using the Brain Extraction Tool (BET) from FSL version 6.0 (https://fsl.fmrib.ox.ac.uk/fsl) (Smith, 2002). In order to achieve an accurate brain extraction given the large deformities present in the dataset, various BET parameters were tuned, and manual removal of non-brain structures was performed following BET on a per subject basis.

2.2.3.2 Bias Correction

Bias correction to correct for intensity inhomogeneities was performed using N4 bias field correction from ANTs (http://picsl.upenn.edu/software/ants/) (Tustison et al., 2010).

2.2.4 Image Registration

Images were both registered to the 1 x 1 x $1mm^3$ MNI-152 nonlinear 6th generation template. Additionally, images were registered to the NIHPD symmetric pre- to mid-puberty (7.5 years to 13.5 years) 1 x 1 x $1mm^3$ pediatric template, followed by registration to the aforementioned MNI-152 template. This additional registration was performed as it has been suggested that registering an age specific template could produce more accurate registrations (Fonov et al., 2011; Wilke et al., 2002). Image registration using the DARTEL Toolbox differed from the aforementioned process, firstly DARTEL creates a groupwise template image wherein each participant's neuroimage is registered to the groupwise template, then these images can be normalized to MNI space.

2.2.4.1 Registration program details

A variety of freely available programs commonly used for neuroimaging analysis were chosen. The selected programs employ a variety of registration algorithms and implementations. All registrations were implemented using default parameters, except for FLIRT wherein two iterations were used, one with the default parameters and a second with a reduced angular range for initial optimization (FLIRT 2 and FNIRT 2 represent linear and non-linear registrations completed with a reduced angular range during the linear registration step). View Table 1 for a list of the programs used, and Appendix A for the settings used.

Table 1: Registration programs assessed

Function, *Program*
Deformable Registration via Attribute Matching and Mutual-Saliency Weighting (DRAMMS), *DRAMMS Deformable Image Registration Toolbox* (https://www.nitrc.org/projects/dramms) (Ou et al., 2011)
Diffeomorphic Anatomical Registration using Exponentiated Lie algebra (DARTEL), *Statistical Parametric Mapping (SPM)* (Ashburner, 2007)
FMRIB's Linear Image Registration Tool (FLIRT), *FMRIB Software Library (FSL)* (Jenkinson et al., 2002)
FMRIB's Non-Linear Image Registration Tool (FNIRT), *FMRIB Software Library (FSL)* (Smith et al., 2004)
Symmetric Image Normalization (SyN), *Advanced Normalization Tools (ANTs)* (http://stnava.github.io/ANTs/) (Avants et al., 2011)

2.2.5 Data analyses

2.2.5.1 Region selection and verification

A series of cortical and subcortical regions were selected to represent areas proximal and distal to the area of deformation as it has been previously demonstrated that registration accuracy can be impacted by proximity to the region of deformation (Ou et al., 2014). Areas included in the custom atlas include the corpus callosum, internal capsule, superior temporal gyrus, hippocampus, superior occipital gyrus, and paracentral lobule (view Figure 5 for the atlas). All areas were manually segmented from each patient's neuroimage as well as the template image and verified by an expert (SdeR). The custom study atlas in each participant's native space was then warped using the generated warps from all registrations for analysis.

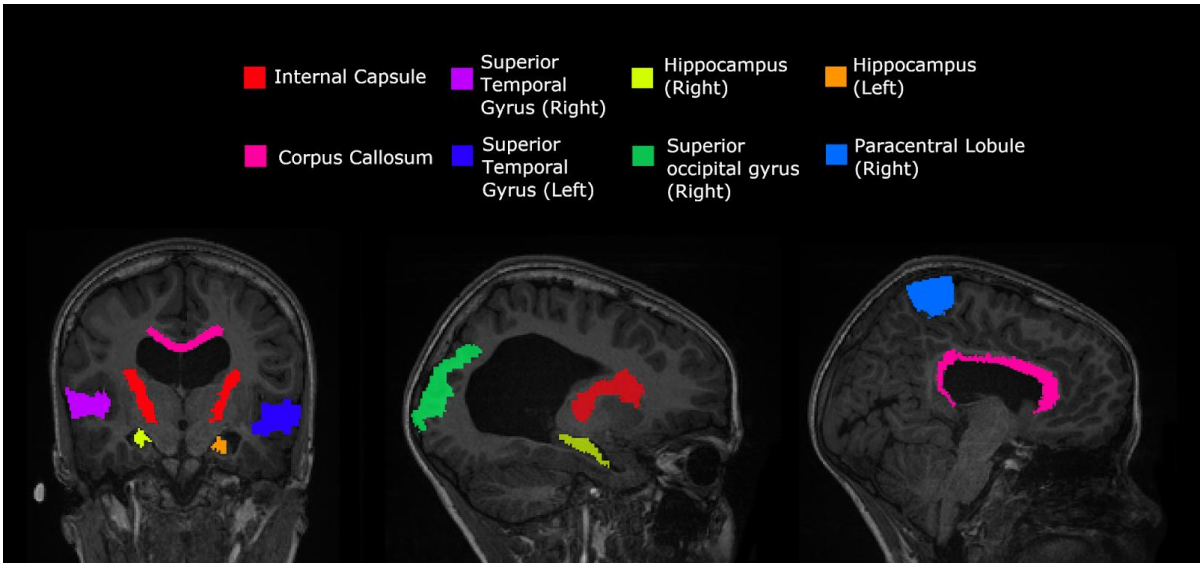

Figure 5: Custom atlas used for registration which includes various cortical and subcortical structures. All selected regions are represented at least once unilaterally.

2.2.5.2 Computational Time

All registrations were performed on a computer with the Linux CentOS version 8 operating system, 64GB of RAM, GeForce 970GTX GPU, and an AMD Ryzen 5 3600 6-Core Processor (3.6GHz/ 4.2 GHz boost). Registration time was reported in minutes, rounded up to the nearest minute. Given that computation time can be influenced by the size of deformation needing to be estimated, computation time for both the most and least deformed brains have been reported. Multi-core processing was used whenever supported by the software tool and the number of cores used was reported.

2.2.5.3 Similarity Metrics

In order to evaluate the accuracy of the registration two commonly reported similarity metrics were used (Taha & Hanbury, 2015). The warped participant atlas was compared to the same areas segmented from the MNI-152 template image. The Dice coefficients (DICE) were computed for each registration to assess similarity in overlap of the selected 3-dimensional regions (Dice, 1945). Using two sets, A and B, the DICE is defined as:

$$DICE = \frac{2\,|(A \cap B)|}{|A| + |B|}$$

Additionally, Hausdorff Distance (HD) which is a measure of spatial distance was also assessed (Hausdorff, 1914). Using two sets, A and B, HD is defined as:

$$HD = max(h(A,B), h(B,A))$$

$$h(A,B) = \max_{a \epsilon A} \min_{b \epsilon B} ||a - b||$$

2.3 Results

2.3.1 Participants

Eight patients with hydrocephalus treated with a VP shunt were included in the current study (1 female, *mean* age = 8.79 years, *sd* = 1.81). Their voxel-based ventricle volume ranged from 6,428 mm^3 to 336,735 mm^3. The etiology of the hydrocephalus was variable between patients, and included intraventricular hemorrhage, dandy-walker's malformation, meningitis, and spina bifida. Complete atlas generation was possible in seven of the eight participants. In the participant with the largest ventricle size severe deformities resulted in the inability to distinguish three cortical regions (i.e., left superior occipital gyrus, and both left and right paracentral lobules).

2.3.2 Normalization

A total of 592 registrations were performed. Excluding the registration of whole-brain bias corrected data, registrations directly to the MNI template had a larger DICE and smaller HD, indicative of a more accurate registration, compared to registering to an age-appropriate template prior to the MNI-152 template.

Overall, normalization performed with the preprocessing steps of both skull-striping and bias correction had a larger DICE (*median DICE* = 0.5810, *IQR* = 0.1740) and smaller HD (*median HD* = 12.2915, *IQR* =5.2510) compared to those normalizations with whole-brain, and non-bias corrected neuroimages. Figure 6 qualitatively shows registrations for skull-stripped bias corrected images.

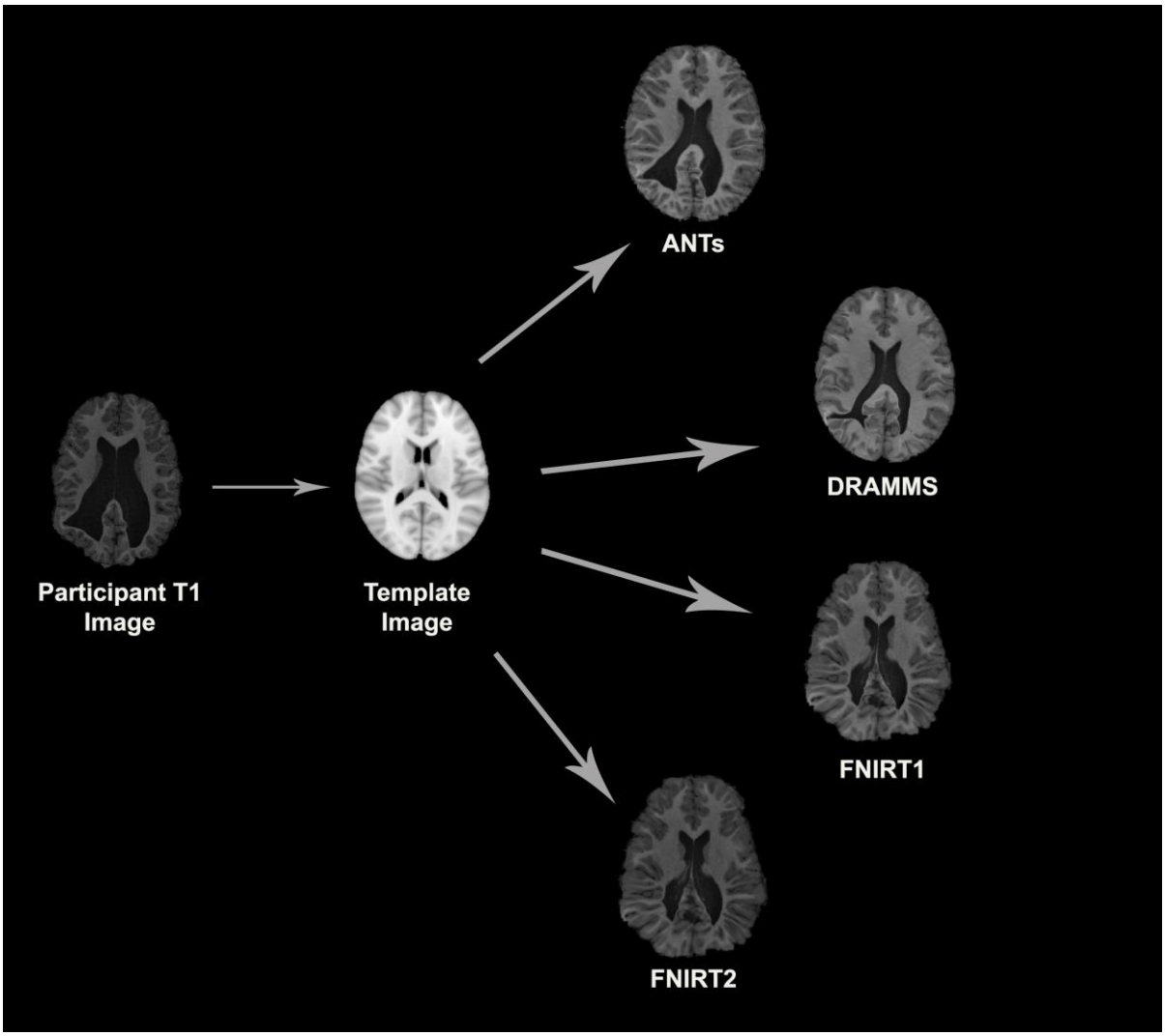

Figure 6: Normalization results for one participant. The participant's neuroimage was skull-stripped and bias corrected prior to undergoing normalization.

A similar pattern was observed in those registered first to an age-appropriate template where the largest DICE (*median DICE* = 0.5637 *IQR* = 0.1900) was observed in images which underwent skull-stripping and bias correction. Table 2 outlines the median DICE and HD for all regions in the study atlas across all programs and the various preprocessing steps. Figure 7 depicts box plots for the DICE score per program and Figure 8 depicts box plots for the HD per program. Both figures use the preprocessing step of bias correction and include results with, and without skull-stripping. The median score for each participant has been shown by ventricle size.

Whether assessed with DICE or HD, the interquartile range is often smaller for bias corrected images that underwent skull-stripping compared to whole brain images for the majority of programs assessed. Additionally, regardless of program and preprocessing performed, patients with the largest ventricle size predominately have poorer registration accuracy compared to those with a smaller ventricle size as measured using DICE. In contrast, when accuracy is measured using HD there is less distinction between accuracy based on ventricle size, though participants with the two largest ventricle sizes (i.e., ventricle size > 100,000 mm^3) often have scores worse than the median.

The better DICE was seen with the SyN algorithm by ANTs with the preprocessing steps of skull-stripping, and bias correction, with or without initial registration to a pediatric atlas (without intermediate registration *median DICE* = 0.6504, *IQR* = 0.1009; *median HD* = 10.3920, *IQR* = 4.9754; with initial registration to a pediatric atlas *median DICE* = 0.6590, *IQR* = 0.1449; *median HD* = 9.4340, *IQR* = 5.7898). Figure 9 (A and B) shows the individual performance for each participant, and each region of interest using the SyN algorithm with bias correction and skull-stripping. As ventricle size increases, overall subcortical regions which are closer to the ventricles, on average, have lower DICE compared to cortical regions. When assessing accuracy using HD, participants with the smallest ventricle sizes (i.e., < 8000 mm^3) predominately have a HD for subcortical structures below the median and an HD for cortical structures above the median.

The best performance with the least number of preprocessing steps (i.e., whole brain, no bias correction) was the DARTEL toolbox by SPM (*median DICE* = 0.5541, *sd* = 0.1604; *median*

HD = 11.5330, *sd* = 5.2630). Similar to SyN, subcortical regions generally have a lower DICE (Figure 9 C) as participant ventricle size increases, compared to cortical regions.

Table 2: Summary statistics for normalization accuracy across 50 registration conditions.

Preprocessing	Similarity Metric	ANTs Median(IQR)	DARTEL Median(IQR)	DRAMMS Median(IQR)	FLIRT *(1)* Median(IQR)	FLIRT *(2)* Median(IQR)	FNIRT *(1)* Median(IQR)	FNIRT *(2)* Median(IQR)	Overall Median(IQR)
T1 to MNI152									
Whole Brain	DICE	0.5102(0.2967)	0.5541(0.1604)	0.4979(0.1796)	0.3957(0.1824)	0.4110(0.1763)	0.5008(0.2074)	0.5205(0.2057)	0.4767(0.2321)
	HD	14.3180(8.7530)	11.5330 (5.2630)	14.3530(6.3730)	14.7990(10.0950)	14.7990 (8.4870)	14.3530(8.4113)	14.8660(8.0610)	14.1770(7.7735)
Whole Brain Bias Corrected	DICE	0.5051(0.3078)	0.5388 (0.1624)	0.4906(0.1521)	0.3568 (0.2304)	0.3857(0.2522)	0.4738(0.2675)	0.4518(0.3846)	0.4506(0.2602)
	HD	15.0330(8.5790)	11.4020(4.7974)	13.5650(7.4310)	15.3950(11.7050)	16.0310(13.0030)	15.8430(11.7800)	16.6130(11.4690)	14.4570(10.3255)
Skull-Stripped	DICE	0.6468(0.1389)	-	0.5991(0.1577)	0.5291(0.1745)	0.5290(0.1769)	0.5765(0.1981)	0.5778(0.1976)	0.5734(0.1852)
	HD	10.6300(5.6240)	-	11.0450(5.0985)	11.3580(4.9522)	11.3580 (4.8062)	11.7900(5.5866)	11.7900(5.6756)	11.1800(5.5638)
Skull-Stripped Bias Corrected	DICE	0.6504 (0.1009)	-	0.5909(0.1571)	0.5201(0.1796)	0.5211(0.1787)	0.5974(0.1617)	0.5969(0.1674)	0.5810(0.1740)
	HD	10.3920(4.9754)	-	11.0910(5.3180)	11.6620(4.9837)	11.7050(5.0917)	11.5760(4.8140)	11.7900(4.8840)	11.2915(5.2510)
T1 to NIHPD, NIHPD to MNI152									
Whole Brain	DICE	0.4928(0.2906)	-	0.4485(0.1737)	0.4480(0.2294)	0.4473(0.2425)	0.4987(0.2521)	0.5039(0.2933)	0.4700(0.2380)
	HD	13.4910(9.2300)	-	15.9370(6.8720)	15.2640(6.6720)	15.2970(6.8540)	15.2640(8.7650)	15.1660(8.0260)	15.2640(7.8088)
Whole Brain Bias Corrected	DICE	0.5303(0.2716)	-	0.4563(0.2033)	0.4438(0.2280)	0.4520(0.2266)	0.4969(0.2383)	0.4950(0.2365)	0.4688(0.2352)
	HD	13.8920(9.1050)	-	14.7650(5.1040)	15.0670(7.1490)	15.2640(7.2100)	14.3180(7.9180)	14.1770(8.2680)	14.5260(7.5223)
Skull-Stripped	DICE	0.6439(0.1753)	-	0.5678(0.1496)	0.5285(0.1838)	0.5261(0.1856)	0.5586(0.2090)	0.5532(0.2092)	0.5584(0.1880)
	HD	10.4400(6.0464)	-	12.0830(6.2298)	11.7470 (5.4107)	11.7470 (5.4862)	13.0380(6.5325)	12.7670(6.2940)	11.8740(5.8348)

Skull-Stripped Bias Corrected	DICE	0.6590(0.1449)	-	0.5678(0.1496)	0.5201(0.1790)	0.5190(0.1819)	0.5719(0.2018)	0.5727(0.2133)	0.5637(0.1900)
	HD	9.4340(5.7898)	-	12.0830(6.2298)	11.7470(4.6544)	11.7470(4.4014)	12.3690(5.7525)	12.6890(5.5520)	11.8950(5.8424)

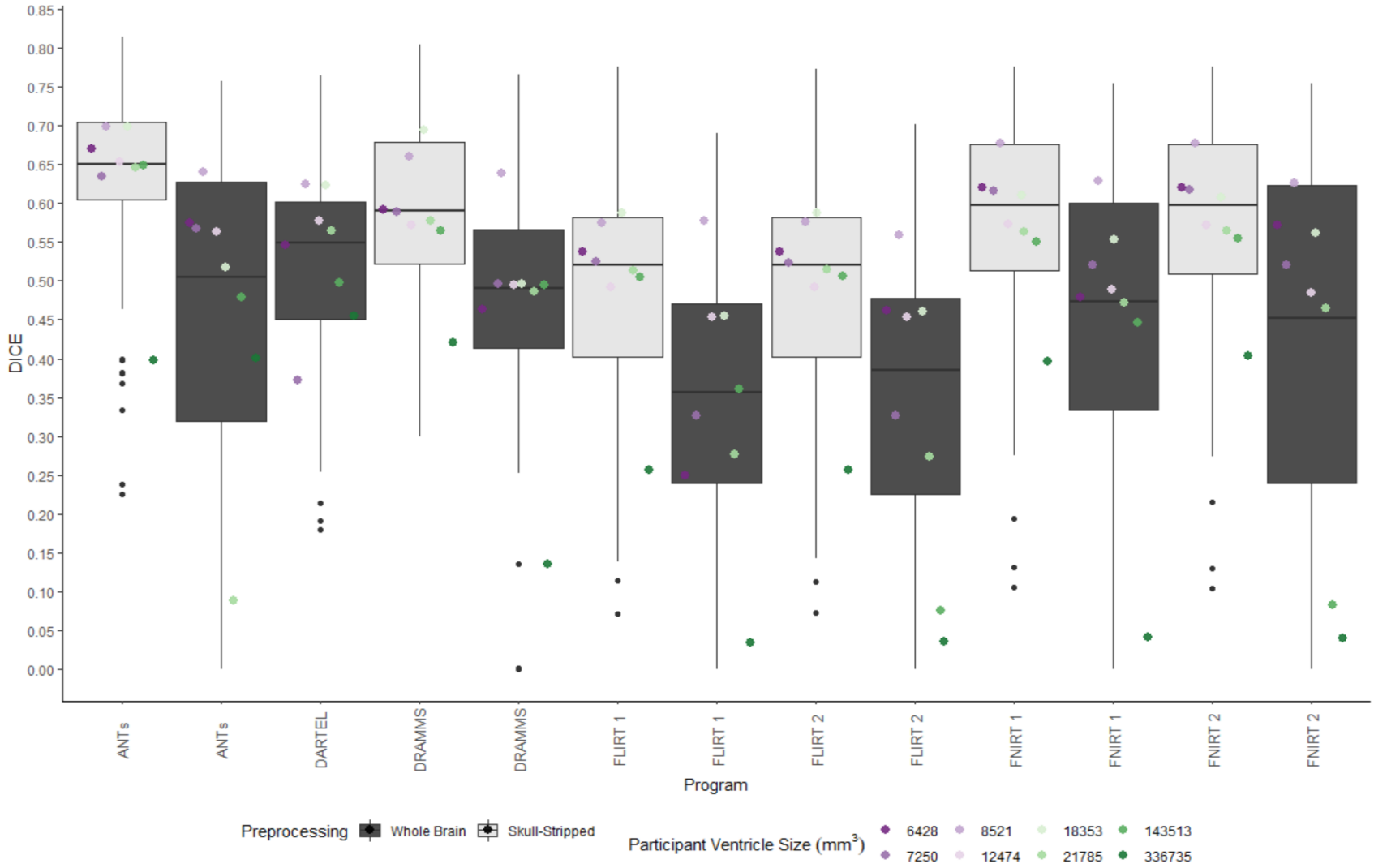

Figure 7: Box plots of the DICE scores per program for normalization from participant T1 to the MNI-152 template image. All images were bias corrected. Results from both whole brain and skull-stripped images are shown in dark gray and light gray respectively. The median DICE per participant is plotted by voxel-wise ventricle size in mm^3.

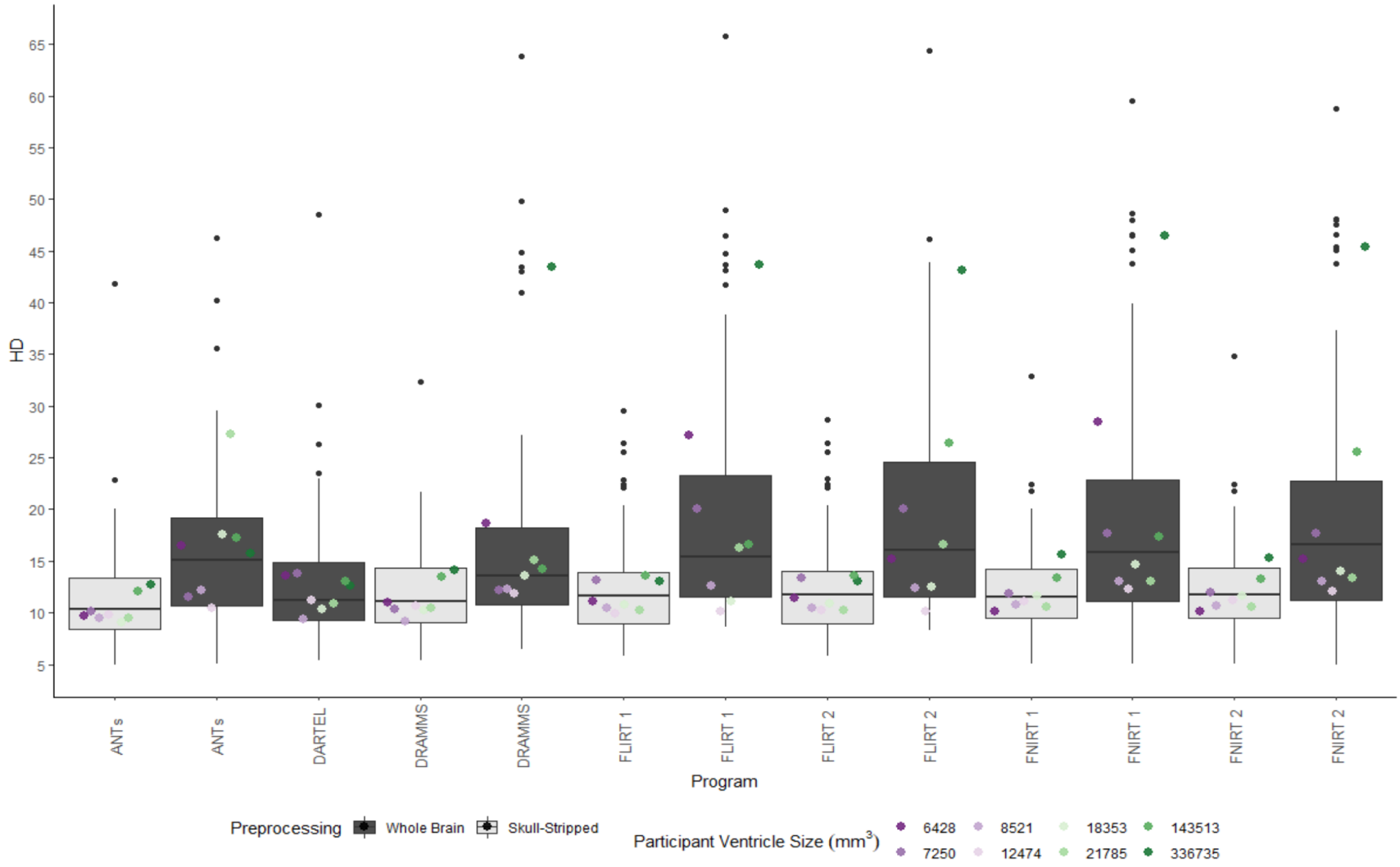

Figure 8: Box plot of the HD per program for normalization from participant T1 to the MNI-152 template image. All images were bias corrected. Results from both whole brain and skull-stripped images are shown in dark gray and light gray respectively. The median HD per participant is plotted by voxel-wise ventricle size in mm^3.

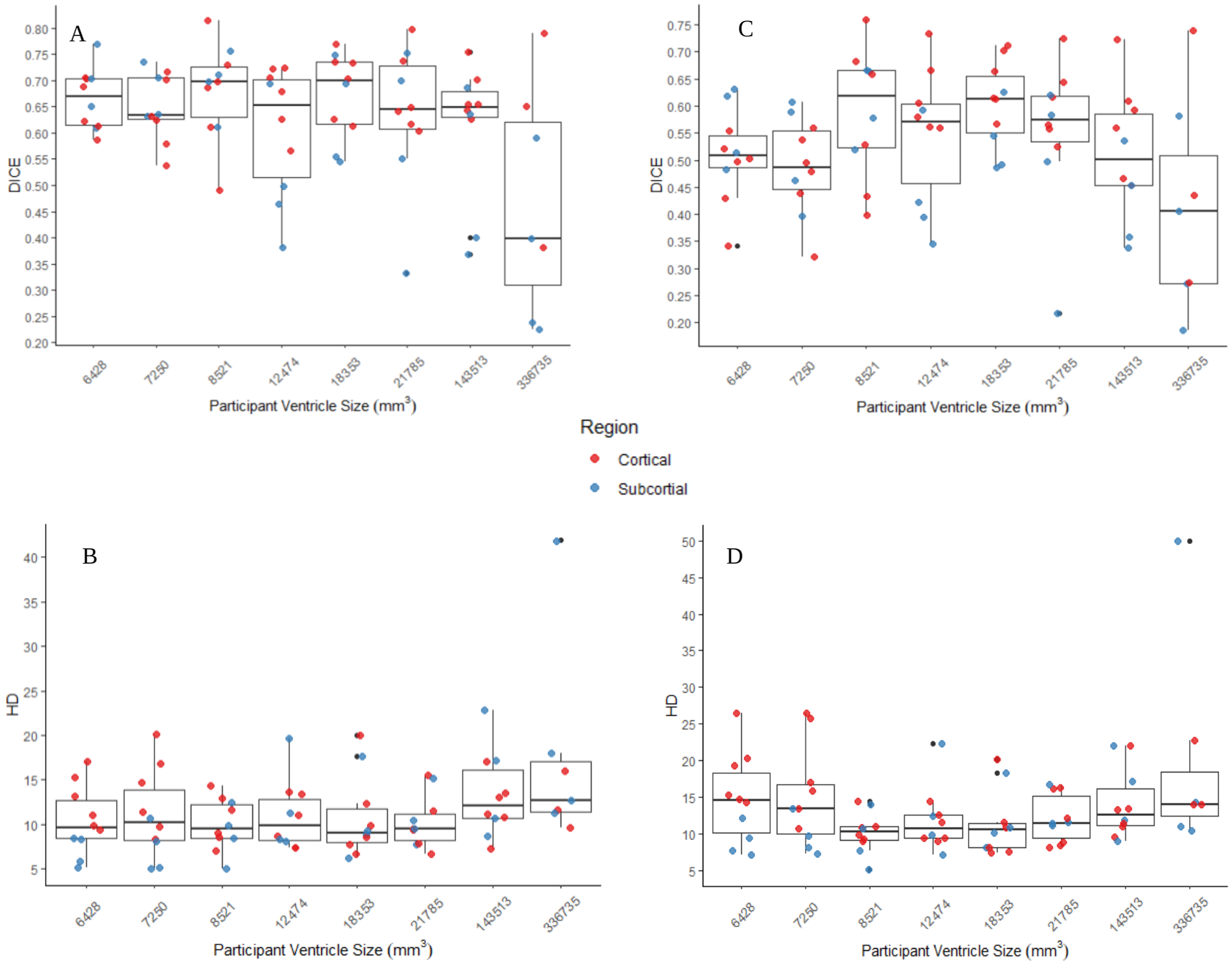
A
C
B
D
DICE
HD
Participant Ventricle Size (mm3)
6428
7250
8521
12474
18353
21785
143513
336735
Region
Cortical
Subcortial

Figure 9: A and B show the DICE score and HD respectively by participant by region for SyN with the preprocessing steps of skull-stripping and bias correction. C and D show the DICE and HD respectively by participant by region for DARTEL with no preprocessing steps (whole-brain, no bias correction). In all graphs, cortical structures are red, and subcortical structures are blue.

2.3.3 Computational Time

Computational time for the smallest and largest ventricle sizes are seen in Table 3. Despite the large differences in ventricle volumes, the time to complete the normalization for either participant are similar except for FNIRT wherein the participant with the smaller ventricle size has a much quicker registration to the MNI-152 template relative to the participant with the larger ventricle size. The fastest non-linear registration is with ANTs with 10 cores (approximately 18 minutes). DRAMMS and FNIRT have comparable times (approximately 20 minutes – 40 minutes) and both use a single-core. Performing two series of registrations from patient T1 to NIHPD, then the registration from the NIHPD atlas to MNI-152 atlas almost increases all the times two-fold which is to be expected as this process involves two-times the registrations. The majority of the algorithms only offer single-core computation. As the DARTEL Toolbox creates a group-wise template, its computational time is dependent on the number of participants. Given the performance of the DARTEL Toolbox with whole-brain non-bias corrected data, this computational time was included.

Table 3: Time to completion for registration

	Smallest ventricle size		**Largest ventricle size**	
	BET Bias corrected (min)	**Pediatric atlas BET Bias corrected (mins)**	**BET Bias corrected (mins)**	**Pediatric atlas BET Bias corrected (mins)**
DRAMMS (single core)	34	83	36	95
FLIRT 1, FSL (single core)	1	2	1	2
FLIRT 2, FSL (single core)	1	2	1	2
FNIRT 1, FSL (single core)	17	64	43	53
FNIRT 2, FSL (single core)	33	63	41	53
SyN, ANTs (single core)	127	273	129	274
SyN, ANTs (10 cores)	18	40	18	39
DARTEL	All participants, whole-brain, no bias correction:			29

2.4 Discussion

Normalization of neuroimages of pediatric patients with shunt-treated hydrocephalus was assessed using a variety of freely available software tools commonly used for neuroimaging studies. Fifty ways of normalizing neuroimages were examined wherein variations included programs, parameters, and preprocessing steps for a total of 592 registrations performed.

Our study revealed that SyN had the most accurate registration as measured by DICE, and HD with, or without registration to a pediatric atlas. Previous studies assessing the accuracy of registration in healthy brains and/or brains with pathologies have also highlighted SyN as registration algorithms that performs with high accuracy (Klein et al., 2009; Ou et al., 2014; Ripolles et al., 2012). In the current study, we found superior registration accuracy using bias corrected, skull-stripped data; however, normalization with non-preprocessed data (i.e., whole-brain, non-bias corrected) can also result in normalized images with good accuracy. Typically, performing bias correction can help to improve normalization accuracy and it is non-computationally intensive relative to the time required to perform registrations. In addition to having a small benefit for normalization, bias correction has been shown to improve brain extraction (Fennema-Notestine et al., 2006). The current dataset composed of pathological pediatric neuroimages revealed that the removal of the skull has been shown to be incredibly beneficial for normalization. However, it is worth noting that skull-stripping has been identified as a non-trivial task which could be very time consuming (Popescu et al., 2012). Poor brain extractions can result in removing areas of the brain or including non-brain matter. Furthermore the presence of neck in the volumes have been shown to negatively impact brain extraction (Popescu et al., 2012). These errors in brain extraction could result in poor registration wherein the non-brain matter for example, could be interpreted as brain matter.

Towards minimizing preprocessing steps, whole brain normalization can also be performed in patients with complex neuropathology, such as that seen in hydrocephalus. It was demonstrated that the DARTEL toolbox outperforms many of the other algorithms under these circumstances. The DARTEL toolbox makes use of groupwise registration and is the only tool assessed in this study which uses this process (Ashburner, 2007). In this case, a group-specific template is created based on the whole input dataset, then each participant's neuroimage is then registered to the group template. Group-wise registrations are beneficial as there is no a priori template selection required; however, performing group-wise registration between different groups (e.g., healthy controls compared to patients with morphological differences) is non-trivial and an area of interest (Liao et al., 2012; Ribbens et al., 2013).

Given the differences between pediatric and adult neuroimages such as the size, shape, and tissue type, it has been previously suggested that using an age-appropriate brain template in registrations, can help to improve registrations reducing the age-based variability between images (Courchesne et al., 2000; Fonov et al., 2011). We have demonstrated that with our current dataset, that registering to an age-appropriate template, for the most part, did not improve registration. Accuracy was similar whether an age-specific template was used, though accuracy was slightly reduced overall. Given the purpose of an age-specific template is to better represent a pediatric brain, structural changes to the brain due to hydrocephalus may make these registrations more difficult (Del Bigio, 2010). In addition, there was almost a two-fold increase in processing time with age-based registration compared to a single registration between the participant's image and the target MNI-152 image, which may not be ideal in some circumstances. Therefore, while we would still advise to register healthy participants with age-specific templates, this step can be skipped when registering children with large anatomical deformation due for example to hydrocephalus.

Regardless of the overall accuracy of the registration (measured using DICE), often, participants with larger ventricle sizes had poorer normalization accuracy compared to those with smaller ventricle sizes. Further, the areas that were most impacted as measured by DICE were those near the ventricles (i.e., subcortical regions) such that these areas have low overlap with ground truth. This observation may be due to the sensitivity of the DICE when comparing regions of different sizes, wherein the size of subcortical structures, particularly the ones chosen, are much smaller in volume compared to the cortical structures. The inclusion of subcortical brain structures in neuroimages studies can be challenging given their small size and many are already excluded from standard atlases (Forstmann et al., 2016). While the subcortical regions assessed in the current study can be considered large relative to other subcortical nuclei, it is possible that DICE was not the best metric to assess volumetric overlap between these regions and ground-truth. Some studies have used a modified DICE, specifically dilated DICE when assessing sub-cortical structures, to reduce the sensitivity to size (Bazin et al., 2020).

Notably, many of the assessed programs do not make use of multicore computing for a single subject. Only SyN allowed a streamline method of utilizing multiple cores by modifying the function call (http://stnava.github.io/ANTs/) (Avants et al., 2009). Improving the computational efficacy of registrations is an area of interest. Given their time-consuming nature, registrations are often performed outside of busy clinical practice, though they have a utility in clinical/surgical practice (Alam et al., 2018). Ultimately, there is ongoing interest in utilizing the power of modern GPUs which are built for parallel processing to improve the computational efficiency of image registration (Shams et al., 2010).

Normalizing images of pediatric patients with shunt-treated hydrocephalus provide a unique opportunity to assess the accuracy of various non-linear registration programs given many different challenges. While the patients in this study had a wide range of ventricle sizes, our study was limited by sample size. Having a larger sample size would potentially allow us to better understand the impact of large deformities on normalization outcomes. Furthermore, as we used a custom atlas for assessing registration accuracy, many regions were excluded. Given a more robust atlas, we could have further assessed the impact of the shunt location on registration accuracy in nearby areas as registration performance can vary based on proximity to a pathological site (Ou et al., 2014). Finally, with the largest DICE being marginally over .60, more robust registration algorithms are needed to better account for complex pathologies.

In sum, we assessed four different non-linear registration algorithms to normalize neuroimages from pediatric patients with shunt-treated hydrocephalus. Ultimately preprocessing the neuroimages to remove non-brain tissue (e.g., skull-striping) and bias correcting resulted in on average the most accurate normalized images using the SyN algorithm. We also demonstrated that the DARTEL Toolbox, which performs a group-wise registration, can produce a similarly accurate registration without any preprocessing steps. Finally, while registering to an age-appropriate atlas has been shown to produce a superior registration outcome, overall it did not have a positive impact on the registration accuracy in the current study. These results may help to inform a normalization pipeline

and algorithm selection for studies with pediatric patients and complex neuronal pathologies.

Chapter 3

3 Altered White Matter Networks, and Associations with Ventricle Volume in Children with Shunt Treated Hydrocephalus

3.1 Introduction

Pediatric hydrocephalus (PH) is a heterogenous neurological disease occurring in approximately 0.1% of births globally (Isaacs et al., 2018). Hydrocephalus is characterized by an abnormally high volume of CSF in the ventricles of the brain, and consequently increased intracranial pressure. This increased pressure could result in compensatory mechanisms in the surrounding tissues, and/or skull as predicted by the Monroe-Kelli Hypothesis (Mokri, 2001; H. L. Rekate, 2020). Treatment for hydrocephalus, such as inserting a shunt or an endoscopic third ventriculostomy, aim to reduce the excess fluid in the ventricles, thereby reducing the intracranial pressure.

Damage to the brain tissues arising from ventricle enlargement can include the stretching of periventricular white matter, myelin loss, and axonal damage (Del Bigio et al., 1994; Del Bigio et al., 2003). Additionally, the association of decreased cerebral blood flow alongside ventriculomegaly is well documented in both preclinical models, and in clinical studies in patients with PH (Hill & Volpe, 1982; Jones et al., 1993; Soul et al., 2000). Decreased blood flow can create a hypoxic environment in the brain and can result in ischemic injuries in the white matter. Notably, even following treatment, the brain tissues that have been damaged due to hydrocephalus may not completely recover, particularly in periventricular areas (Aoyama et al., 2006). While periventricular areas are predominately impacted by hydrocephalus, diffuse effects throughout the brain have also been observed (Yuan et al., 2015). Indeed, it is therefore not surprising that hydrocephalus can result in various neuropsychological dysfunctions including deficits in executive functioning, attention, and visuospatial functioning (see Zielinska, et al., 2017 for a review) (Zielinska et al., 2017).

The extent by which the ventricles decrease in volume following treatment for PH is variable (Hasanin et al., 2020). Further, whether the change in ventricle size indicates

postoperative efficacy is unclear in the literature (Nikas et al., 2014). Recent studies have investigated post-operative ventricle volume as a predictor for white matter integrity, and some have found that larger ventricles were indicative of white matter resembling healthy controls (i.e., increased FA) and, in some cases related to better outcomes (e.g., decreased headaches) (Tan et al., 2018; Williams et al., 2015). It is worth noting however that other studies conflict with these findings and suggest no correlations between ventricle volume and white matter injury (Kulkarni et al., 2015). While the aforementioned studies have explored post-operative ventricle volume as it relates to various diffusion measures (i.e., FA, radial diffusivity [RD], mean diffusivity [MD], and axial diffusivity [AD]), none have taken a whole-brain tractography approach and considered region-to-region connectivity in addition to the diffusion measures across tracts throughout the brain.

The goal of this study was to use a whole-brain connectivity approach to identify white matter networks that differ between children with hydrocephalus and controls using both region-to-region connectivity and white matter diffusion metrics, and assess the association of post-operative ventricle volume with these metrics.

We hypothesize that:

1) There will be differences in white matter microstructure between healthy controls and patients with hydrocephalus.
2) We expect to see both white matter differences locally in the periventricular white matter but also globally, focused predominately in the posterior brain as the occipital horns of the lateral ventricles can dilate quickly, and to a larger extent relative to other areas (Brann et al., 1991; Johnson et al., 1979; Reeder et al., 1983).
3) Finally, we predict, if significant, lateral ventricle volume would be negatively correlated with white matter integrity predominately in posterior areas.

3.2 Methods

3.2.1 Participants

Children with VP shunt-treated hydrocephalus and healthy controls were recruited through a pediatric neurosurgery clinic and the OurBrainsCAN Research Registry respectively. The study protocol was approved by the Western University research ethics board and informed consent and assent was obtained from parents and participants. Participants underwent a behavioural and imaging protocol, and were included in the current study if both the structural and diffusion imaging portion of the protocol were completed. Participants were eligible for the study if they had hydrocephalus within the first two years of life. Additionally, participants were not eligible for the study if they had any MRI contraindications (e.g., a programmable shunt).

3.2.2 Image Acquisition

All neuroimages were acquired using a Siemens MAGNETOM Prisma 3-Tesla MRI scanner with a 32-channel head coil. A T1-weighted image of the whole brain was acquired with the three-dimensional magnetization-prepared rapid gradient-echo (MPRAGE) sequence (Repetition time [TR] = 2300ms ; Echo time [TE] = 2.93ms; Inversion time [TI] = 900ms; Flip Angle = 9° ; Matrix Size = 256 x 256, Number of Slices = 160; Field of View [FOV] = 256mm ; Resolution = 1.0 x 1.0 x 1.0 mm^3). Two consecutive series of diffusion-weighted echo-planar imaging were acquired along 30 gradient directions with a b-value of 1000s/mm^2 (TR = 2500ms; TE 77.40ms; Matrix Size = 192 x 192; Voxel Size = 2.0 x 2.0 x 2.0 mm^3). Images were acquired in reverse phase encoding directions, both anterior to posterior (AP) and posterior to anterior (PA). Further, for each series, one additional image was acquired without diffusion weighting, b-value 0s/mm^2.

3.2.3 Image Processing

3.2.3.1 Diffusion Imaging Preprocessing and Tractography

Diffusion images were preprocessed using both the MRtrix3 software package (https://github.com/MRtrix3/mrtrix3) and FSL version 6.0 (https://fsl.fmrib.ox.ac.uk/fsl)

(Jenkinson et al., 2012; Tournier et al., 2019). A summary of the image processing methods are seen in Figure 10.

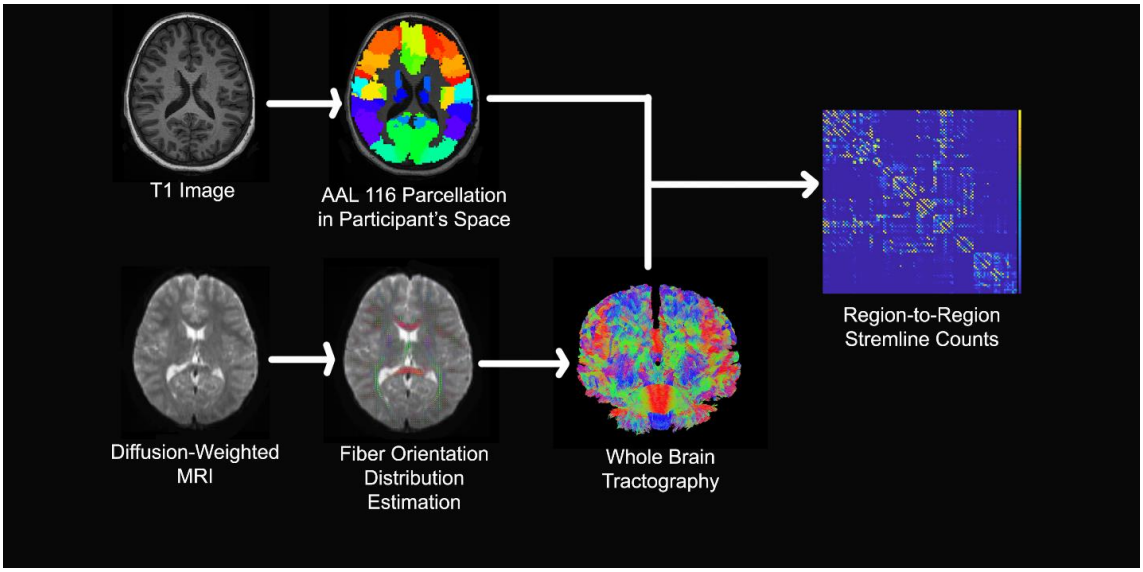

Figure 10: A flow chart summarizing the overarching steps for connectome generation for each participant.

Diffusion images were first denoised using MRtrix3's *dwidenoise* command. The two diffusion weighted imaging runs in the same phase encoding directions were concatenated into one set of data to enhance the signal-to-noise ratio. Afterwards, corrections for motion, eddy current distortion and inhomogeneity distortions were completed using FSL's *eddy* and *topup* commands (Andersson et al., 2003; Andersson & Sotiropoulos, 2016). Using the preprocessed images with a brain mask, the response function was then estimated and was used to perform single-shell single-tissue constrained spherical deconvolution which estimates the fiber orientation distributions (FOD) (Tournier et al., 2007; Tournier et al., 2013). White matter FODs are then normalized to correct for residual intensity inhomogeneities. The participant's T1 was then segmented into 5 tissue types which were registered using FSL's FLIRT to the participant's diffusion space. Using the segmented image, gray matter, white matter boundaries are determined for streamline seed regions. With these seed regions, anatomy constrained probabilistic tractography was performed. Ten million streamlines were generated, the angle value between consecutive steps of 45 was used, and an FOD cut-off

amplitude of 0.15 was used. Anatomy constrained probabilistic tractography was used to improve the biological accuracy of the generated streamlines, furthermore the command *backtrack* was used to allow tracts to be truncated and re-tracked if there was a poor termination (Smith et al., 2012). Following whole-brain tractography, spherical-deconvolution informed filtering of tractograms 2 (SIFT2) was applied to address the connectivity quantification problem and enable quantitative comparisons (Smith et al., 2015).

3.2.3.2 Connectivity Matrices

The Automated Anatomical Labeling (AAL) atlas with 116 regions was used to generate the connectome for each individual patient. Firstly, ANTs (http://picsl.upenn.edu/software/ants/) SyN algorithm was used to transform the AAL atlas from MNI space to the participant's native space using a bias corrected and skull-stripped T1 image as described in Chapter 2 (Avants et al., 2011). Following this registration, the atlas image in the participant's native space was registered to diffusion image using FSL's FLIRT using the previously determined warp. All regions of the AAL atlas were considered nodes wherein a 116 x 116 connectivity matrix was generated. Each element of the matrix represents the SIFT2 scaled streamline count between regions. Similar to other studies (Conti et al., 2017; Pannek et al., 2014) a threshold was applied to the connectome wherein if the mean streamline count across all participants was less than 250, then the tract was not included for further analysis. Using each participant's thresholded streamline count matrix, four other connectivity matrices were generated wherein the weighting for each element is the mean FA, RD, AD, and MD for each tract.

3.2.3.3 Ventricle segmentation

The lateral ventricles were semi-automatically segmented to determine lateral ventricle volume in mm^3. Ventricles were initially automatically segmented using the "recon-all" command from FreeSurfer version 7.1.1 (Athinoula A. Martinos Center for Biomedical Imaging, Harvard-MIT, Boston). Manual adjustments were then made to the segmentations, and the segmentations were verified by an expert (SdeR).

3.2.4 Statistical Analysis

3.2.4.1 Network Based Statistics

In order to assess structural connectivity differences between hydrocephalus patients and healthy controls, network-based statistics (NBS) using the NBS Connectome toolbox (https://www.nitrc.org/projects/nbs/) in MATLAB v2020a (Mathworks Inc. Mattick, USA) was used (Zalesky et al., 2010). NBS is a nonparametric technique that allows for family-wise error control, in a weak sense, when conducting mass univariate testing (see Zalesky et al., 2010 for additional details). The NBS method is a multi-step process: Firstly, a test statistic is computed for each connection in the network based on structural connectivity differences between groups. Following this, supra-threshold connections (i.e., connections with a test statistic greater than a primary threshold) are extracted. The current study used a primary threshold of 3.7 for streamlines and 4.7 for all diffusion metrics. Similar to other studies, at lower primary thresholds larger wide-spread networks were seen, and at very high thresholds, many small isolated networks were found; wherein both these extremes are difficult to interpret (Conti et al., 2017). Using these supra-threshold connections, topological clusters, indicating potential clusters of interest, are determined. To estimate the statistical significance of these clusters of interest, permutation testing is used. Using 5000 random permutations and repeating the previous steps the null distribution of the largest component size is obtained. Then the number of random permutations with larger clusters than the cluster of interest can be compared, wherein the final result is controlled for family-wise error rate at a cluster level with a $p < .05$. Both age and gender were included as a regressor in the NBS model.

3.2.4.2 Regression

For each network discovered using NBS, the individual SIFT2 weighted streamline counts, FA, RD, MD, and AD, for each node edge pairing were further explored using a multiple regression model. Predictors included lateral ventricle volume, and also total brain volume, and age at assessment were included as controls. Multiple comparisons were corrected for using the Holm correction wherein the number of p-values considered are the number of edges in the network. A Holm correct $p < .05$ was considered

significant (Holm, 1979). Regressions were performed using RStudio version 4.1.3 (RStudio Team, 2020).

3.3 Results

3.3.1 Participants

Fifty participants were recruited, 11 patients with VP shunt treated hydrocephalus and 39 healthy controls. Of the initial 50 participants, a total of 44 completed the imaging protocol and were included in the current study. Eight patients with hydrocephalus were included (age in months $\mu(\sigma)$ = 105.50(21.75); 1 female (12.5%)). View Table 4 for hydrocephalus patient details. A total of 36 children were included as healthy controls (age in months $\mu(\sigma)$ = 108.61(32.10); 21 female (58.33%)).

Table 4: Summary of all included hydrocephalus patient demographic information.

Case No.	Age (months)	Gender	Ventricle Size (mm^3)	Shunt Revisions	Premature	Birth weight	Etiology
2A	119	M	8521	0	No	Normal	Intraventricular Hemorrhage
4A	75	M	6428	0	No	Normal	Dandy-Walker's Malformation
4A2	87	M	7250	0	No	Normal	Dandy-Walker's Malformation
5A	107	M	12474	0	Yes	Below normal	Intraventricular Hemorrhage and meningitis
6A	136	M	336735	3	Yes	Below normal	Intraventricular Hemorrhage
7A	121	F	143513	0	No	Normal	Spina Bifida
8A	82	M	18353	0	No	Normal	N/A
9A	117	M	21785	2	No	Normal	Spina Bifida

3.3.2 Streamline Counts

Using NBS we found significant differences for region-to-region streamline counts between healthy controls and patients with hydrocephalus. The four network components were visualized with BrainNet Viewer (Xia et al., 2013, http://www.nitrc.org/projects/bnv/) and are displayed in Figure 11A. and a list of regions pairs in Appendix B.

There were two network components wherein the streamline counts in hydrocephalus patients were less than those found in controls. Network component 1 consisted of 8 nodes, and 7 edges (p = .0006) and predominantly involved connections to the hippocampus, and thalamus. Network component 2 was a smaller network, exclusively on the right hemisphere, consisting of 3 nodes, and 2 edges (p = .0100) predominantly involving connections to the temporal gyrus. In hydrocephalus patients, our regression model did not predict any difference in streamline counts in either of these networks.

There were also two network components where streamline counts were greater for patients with hydrocephalus compared to controls. The first network component was located exclusively in the right hemisphere and involved 4 nodes, and 3 edges (p = .0324). This network was composed of principally connections involving the temporal gyrus and insula. The next network component was large, composed of 13 nodes and 17 edges (p = .002) where all the connections involved cerebellar structures. This network had two edges that were predicted using the regression model, where lateral ventricle volume was a positive predictor; however this was not significant after multiple comparisons (see Table 5 for regression results).

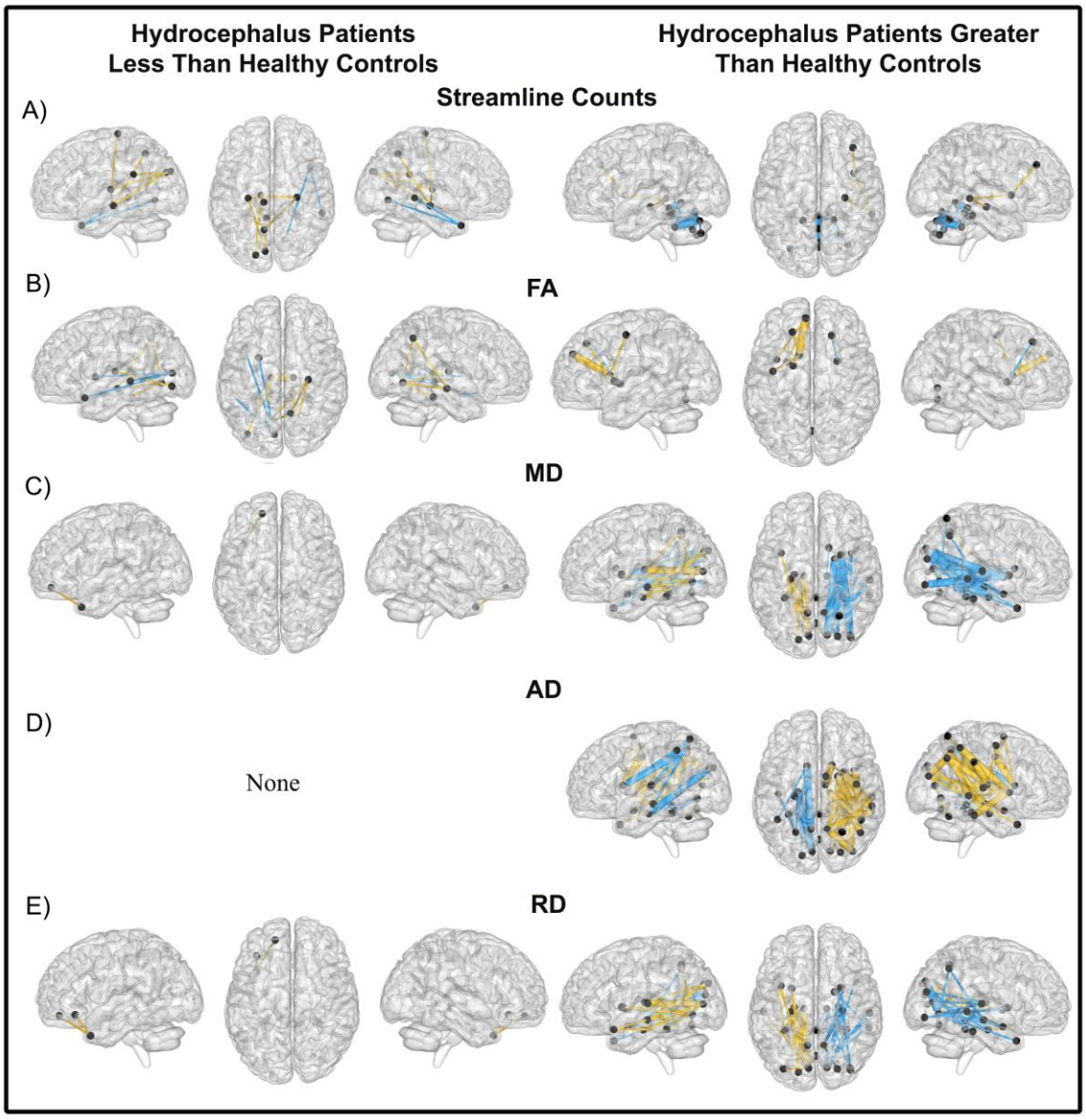
Hydrocephalus Patients
Less Than Healthy Controls
Hydrocephalus Patients Greater
Than Healthy Controls
Streamline Counts
A)
B)
FA
C)
MD
D)
AD
None
E)
RD

Figure 11: Significantly different network components as determined using Network-Based Statistics. Colours depict significantly different network components (yellow = component 1, blue = component 2, pink = component 3). Edge weight depicts the edge metric being predicted by the multiple regression model. Rows depict network components that differ between healthy controls and patients with hydrocephalus in either: A) Streamline count differences where there were 2 networks with both decreased and increased streamline counts. B) FA differences where there were 2 networks with decreased FA, and 3 networks with increased FA. C) MD difference where there was 1 network with decreased MD, and 2 networks with increased MD. D) AD difference where there was 2 networks with increased AD, and E) RD differences where there was 1 network with increased RD and 2 networks with decreased RD.

Table 5: Regression results for tracts that were significant prior to multiple comparisons

Region 1 → Region 2	Regression Model Summary *adjusted* R^2, *F*, *p*	Significant Predictors estimate (standard Error)
Streamline Count		
PH > HC: Network 2		
Vermis_3 → Vermis_4_5	R^2=0.7254, *F*(3,4)=7.164, *p* =.0437	VV: 2.838e-02 (7.183e-03) * WMGM: -2.564e-02 (7.908e-03) *
Cerebelum_6_R → Vermis_7	R^2=0.0.7418, *F*(3,4)=7.702, *p* =.03876	VV: 1.749e-02 (4.899e-03) * Age: -1.133e+02 (2.543e+01) *
Vermis_7 → Vermis_10	R^2=0.7431, *F*(3,4)=7.751, *p* =.03836	Age: -5.971e+01(1.562e+01) *
Fractional Anisotropy		
PH < HC: Network 1		
Thalamus_L → Thalamus_R	R^2=0.8502, *F*(3,4)=14.24, *p* =.01334	Age: -3.405e-03 (6.342e-04) **
HC > PH: Network 1		
Frontal_Sup_Medial_L → Caudate_L	R^2=0.8492, *F*(3,4)=14.14, *p* =.01352	VV: -3.672e-07 (6.102e-08) ** Age: 1.645e-03 (3.168e-04) **
Mean Diffusivity		
PH > HC: Network 1		
Calcarine_L → Thalamus_L†	R^2= 0.9770, *F*(3,4)=100.2, *p* =.0003	VV: 1.783e-09 (1.037e-10) *** Age: -5.552e-06 (5.385e-07) *** WMGM: -4.444e-10 (1.142e-10) *
PH > HC: Network 2		
Cuneus_R → Pallidum_R	R^2=0.8636, *F*(3,4)=15.77 , *p*=.0111	VV: 7.004e-10 (1.230e-10) **
Hippocampus_R → Cuneus_R	R^2=0.8826, *F*(3,4)=18.54 , *p*=.0082	VV: 9.810e-10 (1.752e-10) **
Occipital_Inf_R → Putamen_R	R^2=0.8200, *F*(3,4)=11.63 , *p*=.0191	VV: 7.114e-10 (1.506e-10) **
Axial Diffusivity		
PH > HC: Network 1		
Insula_R → Parietal_Inf_R	R^2=0.8694 , *F*(3,4)=16.53 , *p*=.0102	VV: 6.259e-10 (9.481e-11) ** Age: -2.805e-06 (4.922e-07) **
Hippocampus_R → Angular_R	R^2=0.7712 , *F*(3,4)=8.866 , *p*=.0306	VV: 4.899e-10 (1.537e-10) *
Cingulum_Mid_R → Caudate_R	R^2=0.7061 , *F*(3,4)=6.605 , *p*=.0498	VV: 1.416e-09 (4.396e-10) * Age: -7.999e-06 (2.282e-06) *
Parietal_Inf_R → Pallidum_R	R^2=0.9430 , *F*(3,4)=39.62 , *p*=.0020	VV: 4.651e-10 (4.500e-11) *** Age: -1.251e-06 (2.336e-07) **
Angular_R → Pallidum_R	R^2=0.7102 , *F*(3,4)=6.718 , *p*=.0485	VV: 4.369e-10 (1.109e-10) *
Parietal_Inf_R → Thalamus_R	R^2=0.8620 , *F*(3,4)=15.58 , *p*=.0113	VV: 6.866e-10 (1.207e-10) **
SupraMarginal_R → Thalamus_R	R^2=0.7413 , *F*(3,4)=7.687 , *p*=.0389	VV: 4.375e-10 (1.471e-10) *
SupraMarginal_R → Heschl_R	R^2=0.7626 , *F*(3,4)=8.494 , *p*=.0329	VV: 2.040e-10 (5.097e-11) * Age: -7.718e-07 (2.646e-07) * WMGM: -2.267e-10 (5.612e-11) *
Precuneus_R → Temporal_Mid_R	R^2=0.9329 , *F*(3,4)=33.44 , *p*=.0027	VV: 1.003e-09 (1.283e-10) **
Putamen_R → Temporal_Inf_R	R^2=0.9288 , *F*(3,4)=31.45 , *p*=.0031	VV: 3.929e-10 (5.514e-11) **
PH > HC: Network 2		
ParaHippocampal_L → Cuneus_L†	R^2=0.9372 , *F*(3,4)=35.8 , *p*=.0024	VV: 5.968e-10 (1.179e-10) **
Precuneus_L → Caudate_L	R^2=0.8007 , *F*(3,4)=10.38 , *p*=.0234	VV: 1.172e-09 (2.515e-10) **

Radial Diffusivity		
PH > HC: Network 1		
Calcarine_L → Thalamus_L	R^2=0.8581, F(3,4)=15.13, p =.01196	VV: 1.846e-09 (2.785e-10) ** Age: -5.378e-06 (1.446e-06) *
PH > HC: Network 2		
Cuneus_R → Lingual_R	R^2=0.7345, F(3,4)=7.46, p =.0409	VV: 6.711e-10 (1.756e-10) *

*$p < 0.05$, **$p < 0.01$, *** $p < 0.001$

† Significant at $p < 0.05$ after multiple comparisons

VV: Ventricle volume

WMGM: White matter/gray matter volume

PH: Pediatric Hydrocephalus

HC: Healthy Controls

3.3.3 White Matter Diffusion Metrics

Using NBS there were significant differences for white matter microstructure measures of FA, MD, RD, and AD between patients with hydrocephalus and healthy controls. On a whole, patients with hydrocephalus had large networks with increased MD, RD, and AD relative to controls. Network components are visualized in Figure 11 B through E and a list of regions pairs are found in Appendix B.

There were two network significant network components where mean tract FA was decreased in patients with hydrocephalus relative to controls (Figure 11B). The first network component composed of 8 nodes and 8 edges (p = .0002) predominantly involved tracts with the hippocampus and thalamus. The second network component was smaller, in the left hemisphere, and composed of 4 nodes and 3 edges (p = .0006), wherein all tracts involved the calcarine. There were no significant regressions with these components following multiple comparisons. There were three significant network components where mean tract FA were greater in hydrocephalus patients compared to controls. Two small networks composed of 2 nodes and 1 edge each (both p = .0022), these components did not have any tracts with FA values significantly predicted by the regression model. There was also one larger network components composed of 7 nodes and 6 edges (p = .0002). This network involved many connections with the caudate and the superior frontal gyrus. Using the regression model, the FA of the tract connecting the left medial superior frontal gyrus to the left caudate could be predicted by lateral ventricle volume and age wherein lateral ventricle volume was a negative predictor; however this was not significant following multiple comparisons.

When assessing white matter microstructure using MD (Figure 11C), there was one small network (2 nodes, 1 edge) where patients with hydrocephalus had decreased MD compared to controls (p = .0046); however there were two large networks where the MD in patients were greater than the MD in controls. The first network was composed of 11 nodes and 14 edges (p = .0002) and predominantly involved tracts connected to the hippocampus and parahippocampal gyrus. In this network, the connection between the left calcarine fissure and surrounding cortex, and thalamus was significantly predicted by lateral ventricle volume, age, and brain volume (see Table 5). The second network

component was also large, composed of 23 nodes, and 42 edges ($p = .0002$) where this network was composed of various subcortical and cortical tracts.

When assessing the AD values of the tracts (Figure 11D), there were no significant networks where controls had greater tract AD values compared to patients with hydrocephalus. There were however two very large networks where tract AD values were higher in patients with hydrocephalus. The first network composed of 30 nodes and 42 edges ($p < .0001$) had various tracts composed of connections between subcortical structures, and tracts between subcortical and cortical structures. There were various tracts with AD values that were predicted by the regression model, however none were significant following multiple comparisons (Table 5). The second network component was composed of 13 nodes, and 13 edges ($p < .0001$) and was predominantly composed of tracts connected to the parahippocampal gyrus, caudate, and precuneus. This network had one tract between the left parahippocampal gyrus and left cuneus where AD values were significantly positively predicted by lateral ventricle volume (Table 5).

There was one small network component (3 nodes, 2 edges) where the tract RD values for patients with hydrocephalus were less than controls ($p = .0010$) (Figure 11E). In contrast, there were two very large networks where the tract RD values for hydrocephalus were greater than controls. The first network had 14 nodes, and 20 edges ($p < .0001$). The second network was composed of 20 nodes, and 24 edges ($p < .0001$). Finally, there were 31 tracts that had both increased RD and MD which have been depicted in Figure 12.

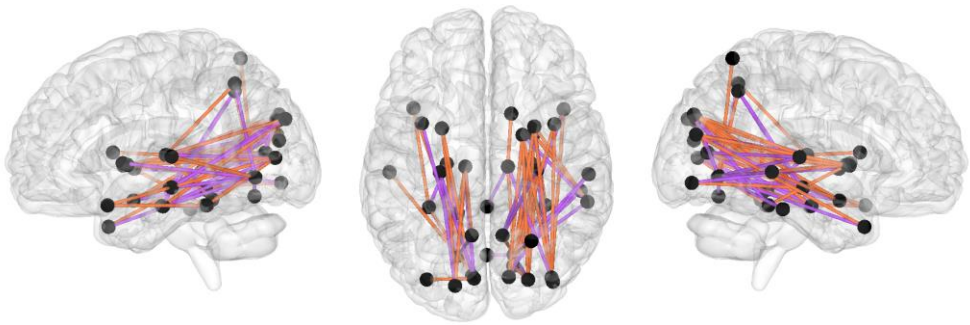

Figure 12: Regions that had either increased RD or increased MD are depicted in orange. Regions that had both increased RD and MD are depicted in purple.

3.4 Discussion

Diffusion imaging allows the exploration and quantification of neuronal white matter. This technique is particularly beneficial when exploring hydrocephalus as it is a disease that greatly impacts white matter. In examining both white matter connectivity using streamline counts and a microstructure approach examining FA, RD, AD, and MD along the tracts connecting regions, we identified differences between white matter for those with pediatric hydrocephalus compared to controls. Consistent with previous studies, we found white matter patterns suggesting decreased white matter integrity in those with hydrocephalus relative to controls (Tan et al., 2018). We have also found some white matter patterns indicative of increase white matter integrity in patients with hydrocephalus relative to controls, which has also been found in other studies throughout the literature (Assaf et al., 2006). Further, we found a small number of tracts whose streamline count or white matter microstructure could be predicted by lateral ventricle volume following corrections for multiple comparisons.

3.4.1 Group-Wise Differences

In taking a whole-brain probabilistic tractography approach, we wanted to assess differences in streamline counts and white matter microstructure. As expected, we found differences between patients with hydrocephalus and controls in both streamline counts and microstructure. Furthermore, the networks that were identified predominately involved posterior structures.

Examining the network that had decreased connectivity as measured by streamline counts in patients with hydrocephalus relative to controls, the network was predominately composed of connections involving the hippocampus and thalamus. Tracts involving the hippocampus and thalamus were common targets of white matter dysregulation as observed in this study wherein many tracts involving these structures also had decreased FA, increased RD, and increased MD. The hippocampus is widely connected throughout the brain, strongly connected to various cortical structures in the temporal, occipital, frontal, and parietal lobes, but also other subcortical structures such as the thalamus (Maller et al., 2019). While the hippocampus is not widely studied in hydrocephalus, a limited number of preclinical studies have demonstrated damaged hippocampal neurons and patterns indicative of reduced cellular connectivity associated with hydrocephalus, as well as impaired performance in spatial learning and memory (Chen et al., 2017; Kriebel & McAllister, 2000). Impaired learning and memory are also seen in children with hydrocephalus relative to health controls. Given the role the hippocampus and its connections including the thalamus have in learning and memory, and the dysregulation of pathways observed in the current study, the hippocampus and its connections should be further studied as it relates to memory and learning in pediatric hydrocephalus.

We also found a large cerebellar network that had an increase in streamline count in patients with hydrocephalus relative to controls, though wide-spread dysregulation of these cerebellar regions were not observed with any of the white matter microstructure measures. Some hydrocephalus etiologies, such as the Dandy-Walker Malformation, Spina Bifida, and Chiari Malformation can impact the shape of the cerebellum. Indeed, as these etiologies were present in many of our participants, it is possible that the differences in streamline counts observed were driven by morphological differences and

an interaction with the tractography, rather than cerebellum related white matter microstructure differences wherein differences would have appeared as well in the tensor metrics.

While many of the networks found in this study were large, some of the smaller networks were centered around a specific node, such as a small network with reduced FA in hydrocephalus patients relative to controls which was centered around the calcarine sulcus. The depth of the calcarine sulcus has been shown to be sensitive to ventriculomegaly of the lateral ventricles wherein larger lateral ventricle volumes are associated with reduced depth of the calcarine sulcus, though no differences were reported for MD values in the occipital lobe (Li et al., 2017; Zhao et al., 2020). Neither of these studies correlated their findings with clinical results; however the calcarine sulcus and surrounding cortex forms the primary visual area, thus neuronal damage in this area could result in difficulties in cognitive visual function. These difficulties have been observed in children with hydrocephalus wherein the difficulties include many different areas including shape recognition, motion perception, and simultaneous perception (Houliston et al., 1999).

On a whole, when assessing white matter microstructure using diffusion metrics of MD, AD, and RD, there were very large networks found wherein the diffusion metrics were higher in hydrocephalus patients relative to controls. All networks were predominately composed of tracts involving exclusively subcortical structures, and regions within the temporal, parietal, and occipital lobes. There was very little involvement of tracts which included frontal regions. This was as expected, given that ventricular dilatation is often quicker in the posterior section of the ventricles, and the occipital horns often dilate further than other areas of the ventricles (Brann et al., 1991; Johnson et al., 1979). While many previous studies have focused on periventricular white matter, taking a whole brain approach, we were able to see broad dysregulation of white matter microstructure, observing increased MD and RD in tracts throughout the occipital lobe and temporal lobe. Notably, distal white matter dysregulation has also been observed in other studies (Tan et al., 2018; Yuan et al., 2015).

Finally, various studies have found white matter dysregulations in both directions, that is, for example relative to controls, patients with hydrocephalus have areas of decreased, as well as increased FA (Assaf et al., 2006; Ben-Sira et al., 2015). We found similar trends when examining FA across the brain, wherein there were both increases and decreases in FA relative to controls. Interestingly we also found a large network with increased AD in patients with hydrocephalus, and no networks with decreased AD in hydrocephalus relative to controls. Many of the tracts that had increased AD, also had increased MD and/or RD. Each of these diffusion metrics can represent a different description of the diffusion tensor wherein FA represents the isotropy of the diffusion, AD the amount of diffusion along the fiber bundle, RD the amount of diffusion perpendicular to the fiber bundle, and MD, the average diffusion over all directions. While increased AD can be indicative of good white matter integrity, it has been suggested that in pathological brains wherein there is increased myelin injury, axonal damage, inflammation and edema, measures of AD and RD are less reliably related to the underlying pathologies (Winklewski et al., 2018). Furthermore, increased AD and RD has been found preoperatively and tends to normalize following surgery (Kim et al., 2011; Scheel et al., 2012). Ultimately, the variations observed in microstructure measures can be for many different reasons, and we cannot know the exact underlying cause; however using multiple metrics we are able to better understand the white matter differences.

3.4.2 Ventricle Volume

In concordance with other studies that have assessed post-operative ventricle volume and its relation to DTI metrics, we also found that ventricle volume was a predictor of various DTI metrics in selective tracts (Tan et al., 2018; Williams et al., 2015). Though most models lost significance following multiple comparisons, two tracts were able to be significantly predicted using our regression model. For the tracts that were significantly predicted by lateral ventricle volume, ventricle volume was a positive predictor, suggesting as ventricle volume increases, as does the tract AD and MD. These significant differences were found in networks wherein those with hydrocephalus have increased values relative to controls, therefore the larger ventricle size is associated with white matter resembling pathological brains as opposed to healthy brains which is in

contraindication to the trends observed in other studies (Tan et al., 2018; Williams et al., 2015). Previous studies have not used a region-to-region tract approach across the whole brain, instead they examined regions of interest or large tracts (e.g., fronto-tectal tracts). Using the region-to-region approach we were able to assess the impact of ventricle volume on specific tracts.

3.4.3 Limitations

The current study is limited by its small sample size. As a result, future studies with larger sample sizes are required to future explore these findings. Given the sample size, we were unable to include predictors in our regression model that may help to predict the white matter streamline and microstructure differences observed in those with hydrocephalus. For example, shunt revisions which reflect shunt failure, and potentially multiple episodes of increased intracranial pressure and ventricular dilatation. Additionally the change in ventricle size between preoperative and postoperative volume would be an interesting predictor. Though we had access to preoperative scans, unfortunately, the majority of the preoperative scans were ultrasound images and as such the volumetric calculations would not be reliable. While postoperative lateral ventricle volume is indicative of the volume at the time of the scan, it does not reflect the previous ventricle size and the potential effect it could have had on the surrounding tissues.

3.5 Conclusion

In summary, we used whole brain probabilistic tractography to assess white matter streamline counts and microstructure metrics in pediatric hydrocephalus patients, and compared tracts in networks that were dysregulated relative to controls with postoperative ventricle size. We found that there were large networks that were dysregulated in hydrocephalus patients which predominately involved tracts with regions outside the frontal lobe. We also found postoperative lateral ventricle volume to be a positive predictor of microstructure metrics in two tracts following correction for multiple comparisons. Additional studies are needed with a larger sample size to allow for a more robust regression model and to further explore the current results.

Chapter 4

4 Conclusions and Future Directions

The current thesis had the objectives to 1) determine what preprocessing steps, and which of the freely available common neuroimaging registration tools would best normalize our sample of brain images from shunt-treated pediatric hydrocephalus patients, and 2) examine the impact of postoperative lateral ventricle volume on white matter structural connectivity across the whole-brain.

In the second chapter of the thesis, we explored various different preprocessing steps and registration algorithms in order to determine which combination of steps and tools would result in the most accurate normalization. While similar studies have been done previously, to my knowledge, this is the first to be completed using patients with shunt-treated pediatric hydrocephalus wherein there are many difficulties associated with registering these images to a standard template. The most accurate registrations were found using SyN from ANTs with the preprocessing steps of skull-stripping (i.e., segmentation of the brain from the skull) and bias correction. While feasible for the current study, a limitation to this approach is the time required to perform the registration using ANTs. Though ANTs allowed for a seamless integration of multicore processing by changing a flag in the command, the time to completion using a single processing core was almost four times as long as the other registration programs. In addition, the skull-stripping step was also non-trivial. Requiring many iterations of tuning parameters and in some cases manually removing remaining segments of skull, this process would likely not be feasible in a busy clinical practice, or with a large sample size. In contrast, the DARTEL toolbox from SPM was found to produce a highly accurate registration without any preprocessing steps completed by the user. Additionally, on our small sample of eight patients the time to completion was approximately half an hour. As DARTEL performs groupwise registration, it would be assumed that as the number of participants increases, as would the time to completion. A benefit of the current study was assessing the registration of both subcortical and cortical structures. Additionally, our sample had a large range of ventricle volumes which provides insight to the accuracy of the registration of these structures in whole-brain studies, like that completed in Chapter 3. Given that, in

many cases, participants with the largest ventricles had decreased registration accuracy relative to those with smaller ventricles, future studies in this area could consider a series of non-parametric tests to see if there is a statistically significant difference. Furthermore, as the ventricles often dilate more posteriorly in hydrocephalus, an examination of the registration of additional posterior structures may provide valuable insight.

The third chapter of the thesis explored the relationship between lateral ventricle volume and white matter diffusion metrics, as well as streamline counts across the whole brain. While only eight participants with hydrocephalus were included, using NBS to control family-wise error, a series of networks were found to be dysregulated in patients with hydrocephalus relative to controls. As expected, many of these networks involved structures close to the ventricles as well as various posterior structures. Following multiple comparisons only white matter metrics in two streamlines were able to be predicted by lateral ventricle volume. The results surrounding the predictive power of ventricle volume further contribute to the conflicted literature. It is possible that taking a NBS approach using all white matter networks as opposed to those dysregulated in hydrocephalus may provide greater insight to the potential impact of postoperative ventricle volume. Given that structures in the frontal lobe were not frequently involved in the dysregulated networks, future studies should continue to focus on periventricular white matter but also consider the impacts of decreased white matter integrity connecting structures in the occipital, temporal and parietal lobes. Examining cognitive and behavioral processes associated with these areas could also help to further understand the impact of these network differences. Similar to other studies we found white matter dysregulation in both directions, wherein there were some networks with increased FA and increased AD relative to healthy controls. Both increases in FA and AD have been shown to normalize following shunt surgery, as a result a regression model that could also include time since last shunt surgery would be beneficial. A benefit to the current study is the use of anatomically constrained tractography wherein streamlines between regions were rejected if they entered the CSF. This process helped to reduce false positives associated with tractography, and attempts to ensure that the streamlines that were generated were biologically plausible. This was particularly relevant in patients with

hydrocephalus as it ensured that there were no streamlines generated in the shunt, or in the ventricles.

In summary, there are challenges in working with neuroimages from patients with pediatric hydrocephalus. The current thesis demonstrates that some registration programs allow better accuracy compared to others. Furthermore, using methods such as anatomy-constrained tractography and NBS, we were able to identify a series of dysregulated networks, many with decreased white matter integrity relative to controls, though there were very few streamlines with white matter metrics that were able to be predicted by postoperative lateral ventricle volume. These results help to inform neuroimaging processing decisions when working with this population and possibly similar populations with large deformities. Furthermore we demonstrated distal impacts on white matter connections providing areas to study further in the future.

References

Alam, F., Rahman, S. U., Ullah, S., & Gulati, K. (2018). Medical image registration in image guided surgery: Issues, challenges and research opportunities. *Biocybernetics and Biomedical Engineering, 38*(1), 71-89.

Andersson, J. L., Skare, S., & Ashburner, J. (2003). How to correct susceptibility distortions in spin-echo echo-planar images: application to diffusion tensor imaging. *Neuroimage, 20*(2), 870-888.

Andersson, J. L., & Sotiropoulos, S. N. (2016). An integrated approach to correction for off-resonance effects and subject movement in diffusion MR imaging. *Neuroimage, 125*, 1063-1078.

Aoyama, Y., Kinoshita, Y., Yokota, A., & Hamada, T. (2006, May). Neuronal damage in hydrocephalus and its restoration by shunt insertion in experimental hydrocephalus: a study involving the neurofilament-immunostaining method. *J Neurosurg, 104*(5 Suppl), 332-339. https://doi.org/10.3171/ped.2006.104.5.332

Ashburner, J. (2007). A fast diffeomorphic image registration algorithm. *NeuroImage, 38*(1), 95-113.

Assaf, Y., Ben-Sira, L., Constantini, S., Chang, L. C., & Beni-Adani, L. (2006, Sep). Diffusion tensor imaging in hydrocephalus: initial experience. *AJNR Am J Neuroradiol, 27*(8), 1717-1724.

Avants, B. B., Tustison, N., & Song, G. (2009). Advanced normalization tools (ANTS). *Insight j, 2*(365), 1-35.

Avants, B. B., Tustison, N. J., Song, G., Cook, P. A., Klein, A., & Gee, J. C. (2011). A reproducible evaluation of ANTs similarity metric performance in brain image registration. *Neuroimage, 54*(3), 2033-2044.

Bach, M., Laun, F. B., Leemans, A., Tax, C. M., Biessels, G. J., Stieltjes, B., & Maier-Hein, K. H. (2014, Oct 15). Methodological considerations on tract-based spatial statistics (TBSS). *Neuroimage, 100*, 358-369. https://doi.org/10.1016/j.neuroimage.2014.06.021

Bazin, P. L., Alkemade, A., Mulder, M. J., Henry, A. G., & Forstmann, B. U. (2020, Dec 16). Multi-contrast anatomical subcortical structures parcellation. *Elife, 9*. https://doi.org/10.7554/eLife.59430

Ben-Sira, L., Goder, N., Bassan, H., Lifshits, S., Assaf, Y., & Constantini, S. (2015, Aug). Clinical benefits of diffusion tensor imaging in hydrocephalus. *J Neurosurg Pediatr, 16*(2), 195-202. https://doi.org/10.3171/2014.10.PEDS13668

Beni-Adani, L., Biani, N., Ben-Sirah, L., & Constantini, S. (2006). The occurrence of obstructive vs absorptive hydrocephalus in newborns and infants: relevance to treatment choices. *Child's Nervous System, 22*(12), 1543-1563.

Bir, S. C., Patra, D. P., Maiti, T. K., Sun, H., Guthikonda, B., Notarianni, C., & Nanda, A. (2016). Epidemiology of adult-onset hydrocephalus: institutional experience with 2001 patients. *Neurosurgical focus, 41*(3), E5.

Boragina, M., & Cohen, E. (2006, Oct 10). An infant with the "setting-sun" eye phenomenon. *CMAJ, 175*(8), 878. https://doi.org/10.1503/cmaj.060507

Brann, B. S. t., Qualls, C., Wells, L., & Papile, L. (1991, Jan). Asymmetric growth of the lateral cerebral ventricle in infants with posthemorrhagic ventricular dilation. *J Pediatr, 118*(1), 108-112. https://doi.org/10.1016/s0022-3476(05)81859-1

Brett, M., Leff, A. P., Rorden, C., & Ashburner, J. (2001, Aug). Spatial normalization of brain images with focal lesions using cost function masking. *NeuroImage, 14*(2), 486-500. https://doi.org/10.1006/nimg.2001.0845

Chen, L. J., Wang, Y. J., Chen, J. R., & Tseng, G. F. (2017, Jul). Hydrocephalus compacted cortex and hippocampus and altered their output neurons in association with spatial learning and memory deficits in rats. *Brain Pathol, 27*(4), 419-436. https://doi.org/10.1111/bpa.12414

Clarençon, F., Bardinet, É., Martinerie, J., Pelbarg, V., Menjot de Champfleur, N., Gupta, R., Tollard, E., Soto-Ares, G., Ibarrola, D., & Schmitt, E. (2017). Lesions in deep gray nuclei after severe traumatic brain injury predict neurologic outcome. *PLoS One, 12*(11), e0186641.

Conti, E., Mitra, J., Calderoni, S., Pannek, K., Shen, K. K., Pagnozzi, A., Rose, S., Mazzotti, S., Scelfo, D., Tosetti, M., Muratori, F., Cioni, G., & Guzzetta, A. (2017, May). Network over-connectivity differentiates autism spectrum disorder from other developmental disorders in toddlers: A diffusion MRI study. *Hum Brain Mapp, 38*(5), 2333-2344. https://doi.org/10.1002/hbm.23520

Courchesne, E., Chisum, H. J., Townsend, J., Cowles, A., Covington, J., Egaas, B., Harwood, M., Hinds, S., & Press, G. A. (2000, Sep). Normal brain development and aging: quantitative analysis at in vivo MR imaging in healthy volunteers. *Radiology, 216*(3), 672-682. https://doi.org/10.1148/radiology.216.3.r00au37672

Crinion, J., Ashburner, J., Leff, A., Brett, M., Price, C., & Friston, K. (2007, Sep 1). Spatial normalization of lesioned brains: performance evaluation and impact on fMRI analyses. *Neuroimage, 37*(3), 866-875. https://doi.org/10.1016/j.neuroimage.2007.04.065

da Silva, M. C., Michowicz, S., Drake, J. M., Chumas, P. D., & Tuor, U. I. (1995, Nov). Reduced local cerebral blood flow in periventricular white matter in experimental neonatal hydrocephalus-restoration with CSF shunting. *J Cereb Blood Flow Metab, 15*(6), 1057-1065. https://doi.org/10.1038/jcbfm.1995.132

Dandy, W. E. (1919). Experimental hydrocephalus. *Annals of surgery, 70*(2), 129.

Del Bigio, M. R. (1993, 1993/05/01). Neuropathological changes caused by hydrocephalus. *Acta Neuropathologica, 85*(6), 573-585. https://doi.org/10.1007/BF00334666

Del Bigio, M. R. (2010). Neuropathology and structural changes in hydrocephalus. *Dev Disabil Res Rev, 16*(1), 16-22. https://doi.org/10.1002/ddrr.94

Del Bigio, M. R., da Silva, M. C., Drake, J. M., & Tuor, U. I. (1994, Nov). Acute and chronic cerebral white matter damage in neonatal hydrocephalus. *Can J Neurol Sci, 21*(4), 299-305. https://doi.org/10.1017/s0317167100040865

Del Bigio, M. R., Wilson, M. J., & Enno, T. (2003, Mar). Chronic hydrocephalus in rats and humans: white matter loss and behavior changes. *Ann Neurol, 53*(3), 337-346. https://doi.org/10.1002/ana.10453

Dewan, M. C., Rattani, A., Mekary, R., Glancz, L. J., Yunusa, I., Baticulon, R. E., Fieggen, G., Wellons, J. C., Park, K. B., & Warf, B. C. (2018, Apr 1). Global hydrocephalus epidemiology and incidence: systematic review and meta-analysis. *J Neurosurg*, 1-15. https://doi.org/10.3171/2017.10.JNS17439

Dice, L. R. (1945). Measures of the amount of ecologic association between species. *Ecology, 26*(3), 297-302.

Ellington, E., & Margolis, G. (1969). Block of arachnoid villus by subarachnoid hemorrhage. *Journal of Neurosurgery, 30*(6), 651-657.

Evans, A. C., Collins, D. L., Mills, S., Brown, E. D., Kelly, R. L., & Peters, T. M. (1993). 3D statistical neuroanatomical models from 305 MRI volumes. 1993 IEEE conference record nuclear science symposium and medical imaging conference,

Feldman, H. M., Yeatman, J. D., Lee, E. S., Barde, L. H., & Gaman-Bean, S. (2010, May). Diffusion tensor imaging: a review for pediatric researchers and clinicians. *J Dev Behav Pediatr, 31*(4), 346-356. https://doi.org/10.1097/DBP.0b013e3181dcaa8b

Fennema-Notestine, C., Ozyurt, I. B., Clark, C. P., Morris, S., Bischoff-Grethe, A., Bondi, M. W., Jernigan, T. L., Fischl, B., Segonne, F., & Shattuck, D. W. (2006). Quantitative evaluation of automated skull-stripping methods applied to contemporary and legacy images: Effects of diagnosis, bias correction, and slice location. *Human brain mapping, 27*(2), 99-113.

Flannery, A. M., Mazzola, C. A., Klimo, P., Duhaime, A.-C., Baird, L. C., Tamber, M. S., Limbrick, D. D., Nikas, D. C., Kemp, J., & Post, A. F. (2014). Foreword: pediatric hydrocephalus: systematic literature review and evidence-based guidelines. *Journal of Neurosurgery: Pediatrics, 14*(Supplement_1), 1-2.

Fletcher, J. M., McCauley, S. R., Brandt, M. E., Bohan, T. P., Kramer, L. A., Francis, D. J., Thorstad, K., & Brookshire, B. L. (1996, Jun). Regional brain tissue composition in children with hydrocephalus. Relationships with cognitive development. *Arch Neurol, 53*(6), 549-557. https://doi.org/10.1001/archneur.1996.00550060093022

Fonov, V., Evans, A. C., Botteron, K., Almli, C. R., McKinstry, R. C., Collins, D. L., & Brain Development Cooperative, G. (2011, Jan 1). Unbiased average age-appropriate atlases for pediatric studies. *Neuroimage, 54*(1), 313-327. https://doi.org/10.1016/j.neuroimage.2010.07.033

Forstmann, B. U., de Hollander, G., van Maanen, L., Alkemade, A., & Keuken, M. C. (2016, Dec 15). Towards a mechanistic understanding of the human subcortex. *Nat Rev Neurosci, 18*(1), 57-65. https://doi.org/10.1038/nrn.2016.163

Giedd, J. N., & Rapoport, J. L. (2010). Structural MRI of pediatric brain development: what have we learned and where are we going? *Neuron, 67*(5), 728-734.

Hanak, B. W., Bonow, R. H., Harris, C. A., & Browd, S. R. (2017). Cerebrospinal Fluid Shunting Complications in Children. *Pediatr Neurosurg, 52*(6), 381-400. https://doi.org/10.1159/000452840

Hanlo, P. W., Gooskens, R. M., Van Schooneveld, M., Tulleken, C. F., van der Knaap, M. S., Faber, J. J., & Willemse, J. (1997). The effect of intracranial pressure on myelination and the relationship with neurodevelopment in infantile hydrocephalus. *Developmental Medicine & Child Neurology, 39*(5), 286-291.

Hasan, K. M., Eluvathingal, T. J., Kramer, L. A., Ewing-Cobbs, L., Dennis, M., & Fletcher, J. M. (2008, Apr). White matter microstructural abnormalities in children with spina bifida myelomeningocele and hydrocephalus: a diffusion tensor tractography study of the association pathways. *J Magn Reson Imaging, 27*(4), 700-709. https://doi.org/10.1002/jmri.21297

Hasanin, T. M., Mansour, A. S., Alemam, S. E., Alnoamany, H. A.-E., & Alam-Eldien, M. L. (2020). Ventricular volume changes after successful shunting in hydrocephalic infants. *Egyptian Journal of Neurosurgery, 35*(1), 1-5.

Hausdorff, F. (1914). *Grundzüge der Mengenlehre*. Viet, Leipzig.

Hellier, P., Barillot, C., Corouge, I., Gibaud, B., Le Goualher, G., Collins, D. L., Evans, A., Malandain, G., Ayache, N., Christensen, G. E., & Johnson, H. J. (2003, Sep). Retrospective evaluation of intersubject brain registration. *IEEE Trans Med Imaging, 22*(9), 1120-1130. https://doi.org/10.1109/TMI.2003.816961

Hill, A., & Volpe, J. J. (1982, Jan). Decrease in pulsatile flow in the anterior cerebral arteries in infantile hydrocephalus. *Pediatrics, 69*(1), 4-7.

Holm, S. (1979). A simple sequentially rejective multiple test procedure. *Scandinavian journal of statistics*, 65-70.

Horsfield, M. A., & Jones, D. K. (2002, Nov-Dec). Applications of diffusion-weighted and diffusion tensor MRI to white matter diseases - a review. *NMR Biomed, 15*(7-8), 570-577. https://doi.org/10.1002/nbm.787

Houliston, M. J., Taguri, A. H., Dutton, G. N., Hajivassiliou, C., & Young, D. G. (1999, May). Evidence of cognitive visual problems in children with hydrocephalus: a

structured clinical history-taking strategy. *Dev Med Child Neurol, 41*(5), 298-306. https://doi.org/10.1017/s0012162299000675

Isaacs, A. M., Riva-Cambrin, J., Yavin, D., Hockley, A., Pringsheim, T. M., Jette, N., Lethebe, B. C., Lowerison, M., Dronyk, J., & Hamilton, M. G. (2018). Age-specific global epidemiology of hydrocephalus: systematic review, metanalysis and global birth surveillance. *PLoS One, 13*(10), e0204926.

Jenkinson, M., Bannister, P., Brady, M., & Smith, S. (2002, Oct). Improved optimization for the robust and accurate linear registration and motion correction of brain images. *NeuroImage, 17*(2), 825-841. https://doi.org/10.1016/s1053-8119(02)91132-8

Jenkinson, M., Beckmann, C. F., Behrens, T. E., Woolrich, M. W., & Smith, S. M. (2012). Fsl. *Neuroimage, 62*(2), 782-790.

Jernigan, T. L., & Tallal, P. (1990). Late childhood changes in brain morphology observable with MRI. *Developmental Medicine & Child Neurology, 32*(5), 379-385.

Johnson, M. L., Mack, L. A., Rumack, C. M., Frost, M., & Rashbaum, C. (1979, Sep). B-mode echoencephalography in the normal and high risk infant. *AJR Am J Roentgenol, 133*(3), 375-381. https://doi.org/10.2214/ajr.133.3.375

Jones, H. C., Richards, H. K., Bucknall, R. M., & Pickard, J. D. (1993, May). Local cerebral blood flow in rats with congenital hydrocephalus. *J Cereb Blood Flow Metab, 13*(3), 531-534. https://doi.org/10.1038/jcbfm.1993.69

Kim, M. J., Seo, S. W., Lee, K. M., Kim, S. T., Lee, J. I., Nam, D. H., & Na, D. L. (2011, Sep). Differential diagnosis of idiopathic normal pressure hydrocephalus from other dementias using diffusion tensor imaging. *AJNR Am J Neuroradiol, 32*(8), 1496-1503. https://doi.org/10.3174/ajnr.A2531

Kirkpatrick, M., Engleman, H., & Minns, R. A. (1989, Jan). Symptoms and signs of progressive hydrocephalus. *Arch Dis Child, 64*(1), 124-128. https://doi.org/10.1136/adc.64.1.124

Klein, A., Andersson, J., Ardekani, B. A., Ashburner, J., Avants, B., Chiang, M. C., Christensen, G. E., Collins, D. L., Gee, J., Hellier, P., Song, J. H., Jenkinson, M., Lepage, C., Rueckert, D., Thompson, P., Vercauteren, T., Woods, R. P., Mann, J.

J., & Parsey, R. V. (2009, Jul 1). Evaluation of 14 nonlinear deformation algorithms applied to human brain MRI registration. *Neuroimage, 46*(3), 786-802. https://doi.org/10.1016/j.neuroimage.2008.12.037

Koyama, T., Marumoto, K., Domen, K., & Miyake, H. (2013). White matter characteristics of idiopathic normal pressure hydrocephalus: a diffusion tensor tract-based spatial statistic study. *Neurol Med Chir (Tokyo), 53*(9), 601-608. https://doi.org/10.2176/nmc.oa2012-0307

Kriebel, R. M., & McAllister, P. (2000). Pathology of the hippocampus in experimental feline infantile hydrocephalus. *Neurological research, 22*(1), 29-36.

Kulkarni, A. V., Donnelly, R., Mabbott, D. J., & Widjaja, E. (2015). Relationship between ventricular size, white matter injury, and neurocognition in children with stable, treated hydrocephalus. *Journal of Neurosurgery: Pediatrics, 16*(3), 267-274.

Li, H., Liu, G., Lin, F., & Liang, H. (2017, Jul). Formation of the calcarine sulcus: a potential marker to predict the progression in utero of isolated mild fetal ventriculomegaly. *Medicine (Baltimore), 96*(28), e7506. https://doi.org/10.1097/MD.0000000000007506

Liao, S., Wu, G., & Shen, D. (2012, Oct). A statistical framework for inter-group image registration. *Neuroinformatics, 10*(4), 367-378. https://doi.org/10.1007/s12021-012-9156-z

Maller, J. J., Welton, T., Middione, M., Callaghan, F. M., Rosenfeld, J. V., & Grieve, S. M. (2019, Feb 20). Revealing the Hippocampal Connectome through Super-Resolution 1150-Direction Diffusion MRI. *Sci Rep, 9*(1), 2418. https://doi.org/10.1038/s41598-018-37905-9

Mazziotta, J., Toga, A., Evans, A., Fox, P., Lancaster, J., Zilles, K., Woods, R., Paus, T., Simpson, G., Pike, B., Holmes, C., Collins, L., Thompson, P., MacDonald, D., Iacoboni, M., Schormann, T., Amunts, K., Palomero-Gallagher, N., Geyer, S., Parsons, L., Narr, K., Kabani, N., Le Goualher, G., Boomsma, D., Cannon, T., Kawashima, R., & Mazoyer, B. (2001, Aug 29). A probabilistic atlas and reference system for the human brain: International Consortium for Brain

Mapping (ICBM). *Philos Trans R Soc Lond B Biol Sci, 356*(1412), 1293-1322. https://doi.org/10.1098/rstb.2001.0915

Mazziotta, J. C., Toga, A. W., Evans, A., Fox, P., & Lancaster, J. (1995, Jun). A probabilistic atlas of the human brain: theory and rationale for its development. The International Consortium for Brain Mapping (ICBM). *Neuroimage, 2*(2), 89-101. https://doi.org/10.1006/nimg.1995.1012

Mokri, B. (2001). The Monro–Kellie hypothesis: applications in CSF volume depletion. *Neurology, 56*(12), 1746-1748.

Nikas, D. C., Post, A. F., Choudhri, A. F., Mazzola, C. A., Mitchell, L., Flannery, A. M., Pediatric Hydrocephalus Systematic, R., & Evidence-Based Guidelines Task, F. (2014, Nov). Pediatric hydrocephalus: systematic literature review and evidence-based guidelines. Part 10: Change in ventricle size as a measurement of effective treatment of hydrocephalus. *J Neurosurg Pediatr, 14 Suppl 1*, 77-81. https://doi.org/10.3171/2014.7.PEDS14330

O'Hayon, B. B., Drake, J. M., Ossip, M. G., Tuli, S., & Clarke, M. (1998, Nov). Frontal and occipital horn ratio: A linear estimate of ventricular size for multiple imaging modalities in pediatric hydrocephalus. *Pediatr Neurosurg, 29*(5), 245-249. https://doi.org/10.1159/000028730

Oi, S. (2011, Oct). Classification of hydrocephalus: critical analysis of classification categories and advantages of "Multi-categorical Hydrocephalus Classification" (Mc HC). *Childs Nerv Syst, 27*(10), 1523-1533. https://doi.org/10.1007/s00381-011-1542-6

Ou, Y., Akbari, H., Bilello, M., Da, X., & Davatzikos, C. (2014, Oct). Comparative evaluation of registration algorithms in different brain databases with varying difficulty: results and insights. *IEEE Trans Med Imaging, 33*(10), 2039-2065. https://doi.org/10.1109/TMI.2014.2330355

Ou, Y., Sotiras, A., Paragios, N., & Davatzikos, C. (2011). DRAMMS: Deformable registration via attribute matching and mutual-saliency weighting. *Medical image analysis, 15*(4), 622-639.

Paff, M., Alexandru-Abrams, D., Muhonen, M., & Loudon, W. (2018). Ventriculoperitoneal shunt complications: a review. *Interdisciplinary Neurosurgery, 13*, 66-70.

Pannek, K., Boyd, R. N., Fiori, S., Guzzetta, A., & Rose, S. E. (2014). Assessment of the structural brain network reveals altered connectivity in children with unilateral cerebral palsy due to periventricular white matter lesions. *Neuroimage Clin, 5*, 84-92. https://doi.org/10.1016/j.nicl.2014.05.018

Pannek, K., George, J. M., Boyd, R. N., Colditz, P. B., Rose, S. E., & Fripp, J. (2020). Brain microstructure and morphology of very preterm-born infants at term equivalent age: associations with motor and cognitive outcomes at 1 and 2 years. *Neuroimage, 221*, 117163.

Patel, S. K., Yuan, W., & Mangano, F. T. (2017). Advanced Neuroimaging Techniques in Pediatric Hydrocephalus. *Pediatr Neurosurg, 52*(6), 436-445. https://doi.org/10.1159/000454717

Paulsen, A. H., Lundar, T., & Lindegaard, K.-F. (2015). Pediatric hydrocephalus: 40-year outcomes in 128 hydrocephalic patients treated with shunts during childhood. Assessment of surgical outcome, work participation, and health-related quality of life. *Journal of Neurosurgery: Pediatrics, 16*(6), 633-641.

Popescu, V., Battaglini, M., Hoogstrate, W., Verfaillie, S. C., Sluimer, I., van Schijndel, R. A., van Dijk, B. W., Cover, K. S., Knol, D. L., & Jenkinson, M. (2012). Optimizing parameter choice for FSL-Brain Extraction Tool (BET) on 3D T1 images in multiple sclerosis. *NeuroImage, 61*(4), 1484-1494.

Pople, I. K. (2002, Sep). Hydrocephalus and shunts: what the neurologist should know. *J Neurol Neurosurg Psychiatry, 73 Suppl 1*, i17-22. https://doi.org/10.1136/jnnp.73.suppl_1.i17

Radhakrishnan, R., Brown, B. P., Kralik, S. F., Bain, D., Persohn, S., Territo, P. R., Jea, A., & Karmazyn, B. (2019, Oct). Frontal Occipital and Frontal Temporal Horn Ratios: Comparison and Validation of Head Ultrasound-Derived Indexes With MRI and Ventricular Volumes in Infantile Ventriculomegaly. *AJR Am J Roentgenol, 213*(4), 925-931. https://doi.org/10.2214/AJR.19.21261

Rajagopal, A., Shimony, J. S., McKinstry, R. C., Altaye, M., Maloney, T., Mangano, F. T., Limbrick, D. D., Holland, S. K., Jones, B. V., Simpson, S., Mercer, D., & Yuan, W. (2013, Dec). White matter microstructural abnormality in children with hydrocephalus detected by probabilistic diffusion tractography. *AJNR Am J Neuroradiol, 34*(12), 2379-2385. https://doi.org/10.3174/ajnr.A3737

Redzic, Z. B., Preston, J. E., Duncan, J. A., Chodobski, A., & Szmydynger-Chodobska, J. (2005). The choroid plexus-cerebrospinal fluid system: from development to aging. *Curr Top Dev Biol, 71*, 1-52. https://doi.org/10.1016/S0070-2153(05)71001-2

Reeder, J. D., Kaude, J. V., & Setzer, E. S. (1983, May). The occipital horn of the lateral ventricles in premature infants. An ultrasonographic study. *Eur J Radiol, 3*(2), 148-150.

Rekate, H. L. (2008, Jan 22). The definition and classification of hydrocephalus: a personal recommendation to stimulate debate. *Cerebrospinal Fluid Res, 5*, 2. https://doi.org/10.1186/1743-8454-5-2

Rekate, H. L. (2009, Mar). A contemporary definition and classification of hydrocephalus. *Semin Pediatr Neurol, 16*(1), 9-15. https://doi.org/10.1016/j.spen.2009.01.002

Rekate, H. L. (2020, Aug). Hydrocephalus in infants: the unique biomechanics and why they matter. *Childs Nerv Syst, 36*(8), 1713-1728. https://doi.org/10.1007/s00381-020-04683-7

Rekate, H. L. (2020). Hydrocephalus in infants: the unique biomechanics and why they matter. *Child's Nervous System: Chns: Official Journal of the International Society for Pediatric Neurosurgery*.

Ribbens, A., Hermans, J., Maes, F., Vandermeulen, D., & Suetens, P. (2013). Unsupervised segmentation, clustering, and groupwise registration of heterogeneous populations of brain MR images. *IEEE transactions on medical imaging*, *33*(2), 201-224.

Ripolles, P., Marco-Pallares, J., de Diego-Balaguer, R., Miro, J., Falip, M., Juncadella, M., Rubio, F., & Rodriguez-Fornells, A. (2012, Apr 2). Analysis of automated

methods for spatial normalization of lesioned brains. *NeuroImage, 60*(2), 1296-1306. https://doi.org/10.1016/j.neuroimage.2012.01.094

Rizvi, R., & Anjum, Q. (2005). Hydrocephalus in children. *The Journal of the Pakistan Medical Association, 55*(11), 502.

RStudio Team. (2020). *Integrated Development for R.* In RStudio, Inc. http://www.rstudio.com/

Scheel, M., Diekhoff, T., Sprung, C., & Hoffmann, K. T. (2012, Sep). Diffusion tensor imaging in hydrocephalus--findings before and after shunt surgery. *Acta Neurochir (Wien), 154*(9), 1699-1706. https://doi.org/10.1007/s00701-012-1377-2

Scholl, I., Aach, T., Deserno, T. M., & Kuhlen, T. (2011). Challenges of medical image processing. *Computer science-Research and development, 26*(1), 5-13.

Shams, R., Sadeghi, P., Kennedy, R. A., & Hartley, R. I. (2010). A survey of medical image registration on multicore and the GPU. *IEEE signal processing magazine, 27*(2), 50-60.

Simon, T. D., Riva-Cambrin, J., Srivastava, R., Bratton, S. L., Dean, J. M., Kestle, J. R., & Hydrocephalus Clinical Research, N. (2008, Feb). Hospital care for children with hydrocephalus in the United States: utilization, charges, comorbidities, and deaths. *J Neurosurg Pediatr, 1*(2), 131-137. https://doi.org/10.3171/PED/2008/1/2/131

Smith, R. E., Tournier, J.-D., Calamante, F., & Connelly, A. (2012). Anatomically-constrained tractography: improved diffusion MRI streamlines tractography through effective use of anatomical information. *Neuroimage, 62*(3), 1924-1938.

Smith, R. E., Tournier, J.-D., Calamante, F., & Connelly, A. (2015). SIFT2: Enabling dense quantitative assessment of brain white matter connectivity using streamlines tractography. *Neuroimage, 119*, 338-351.

Smith, S. M. (2002). Fast robust automated brain extraction. *Human brain mapping, 17*(3), 143-155.

Smith, S. M., Jenkinson, M., Johansen-Berg, H., Rueckert, D., Nichols, T. E., Mackay, C. E., Watkins, K. E., Ciccarelli, O., Cader, M. Z., Matthews, P. M., & Behrens, T. E. (2006, Jul 15). Tract-based spatial statistics: voxelwise analysis of multi-

subject diffusion data. *Neuroimage, 31*(4), 1487-1505. https://doi.org/10.1016/j.neuroimage.2006.02.024

Smith, S. M., Jenkinson, M., Woolrich, M. W., Beckmann, C. F., Behrens, T. E., Johansen-Berg, H., Bannister, P. R., De Luca, M., Drobnjak, I., & Flitney, D. E. (2004). Advances in functional and structural MR image analysis and implementation as FSL. *NeuroImage, 23*, S208-S219.

Soul, J. S., Taylor, G. A., Wypij, D., Duplessis, A. J., & Volpe, J. J. (2000, Oct). Noninvasive detection of changes in cerebral blood flow by near-infrared spectroscopy in a piglet model of hydrocephalus. *Pediatr Res, 48*(4), 445-449. https://doi.org/10.1203/00006450-200010000-00005

Spector, R., Robert Snodgrass, S., & Johanson, C. E. (2015, Nov). A balanced view of the cerebrospinal fluid composition and functions: Focus on adult humans. *Exp Neurol, 273*, 57-68. https://doi.org/10.1016/j.expneurol.2015.07.027

Stone, J. J., Walker, C. T., Jacobson, M., Phillips, V., & Silberstein, H. J. (2013). Revision rate of pediatric ventriculoperitoneal shunts after 15 years. *Journal of Neurosurgery: Pediatrics, 11*(1), 15-19.

Taha, A. A., & Hanbury, A. (2015, Aug 12). Metrics for evaluating 3D medical image segmentation: analysis, selection, and tool. *BMC Med Imaging, 15*, 29. https://doi.org/10.1186/s12880-015-0068-x

Talairach, J. (1988). Co-planar stereotaxic atlas of the human brain-3-dimensional proportional system. *An approach to cerebral imaging*.

Tan, K., Meiri, A., Mowrey, W. B., Abbott, R., Goodrich, J. T., Sandler, A. L., Suri, A. K., Lipton, M. L., & Wagshul, M. E. (2018). Diffusion tensor imaging and ventricle volume quantification in patients with chronic shunt-treated hydrocephalus: a matched case-control study. *Journal of Neurosurgery, 129*(6), 1611-1622.

Tang, Z., Wu, Y., & Fan, Y. (2017, Aug 4). Groupwise registration of MR brain images with tumors. *Phys Med Biol, 62*(17), 6853-6868. https://doi.org/10.1088/1361-6560/aa7c41

Tournier, J.-D., Calamante, F., & Connelly, A. (2007). Robust determination of the fibre orientation distribution in diffusion MRI: non-negativity constrained super-resolved spherical deconvolution. *Neuroimage, 35*(4), 1459-1472.

Tournier, J.-D., Smith, R., Raffelt, D., Tabbara, R., Dhollander, T., Pietsch, M., Christiaens, D., Jeurissen, B., Yeh, C.-H., & Connelly, A. (2019). MRtrix3: A fast, flexible and open software framework for medical image processing and visualisation. *Neuroimage, 202*, 116137.

Tournier, J. D., Calamante, F., & Connelly, A. (2013). Determination of the appropriate b value and number of gradient directions for high-angular-resolution diffusion-weighted imaging. *NMR in Biomedicine, 26*(12), 1775-1786.

Tuli, S., O'Hayon, B., Drake, J., Clarke, M., & Kestle, J. (1999, Dec). Change in ventricular size and effect of ventricular catheter placement in pediatric patients with shunted hydrocephalus. *Neurosurgery, 45*(6), 1329-1333; discussion 1333-1325. https://doi.org/10.1097/00006123-199912000-00012

Tully, H. M., & Dobyns, W. B. (2014, Aug). Infantile hydrocephalus: a review of epidemiology, classification and causes. *Eur J Med Genet, 57*(8), 359-368. https://doi.org/10.1016/j.ejmg.2014.06.002

Tustison, N. J., Avants, B. B., Cook, P. A., Zheng, Y., Egan, A., Yushkevich, P. A., & Gee, J. C. (2010). N4ITK: improved N3 bias correction. *IEEE transactions on medical imaging, 29*(6), 1310-1320.

Vinchon, M., Rekate, H., & Kulkarni, A. V. (2012, Aug 27). Pediatric hydrocephalus outcomes: a review. *Fluids Barriers CNS, 9*(1), 18. https://doi.org/10.1186/2045-8118-9-18

Welker, K. M., & Patton, A. (2012). Assessment of normal myelination with magnetic resonance imaging. Seminars in neurology,

Wilke, M., Schmithorst, V. J., & Holland, S. K. (2002, Sep). Assessment of spatial normalization of whole-brain magnetic resonance images in children. *Hum Brain Mapp, 17*(1), 48-60. https://doi.org/10.1002/hbm.10053

Williams, V. J., Juranek, J., Stuebing, K. K., Cirino, P. T., Dennis, M., Bowman, R. M., Blaser, S., Kramer, L. A., & Fletcher, J. M. (2015). Postshunt lateral ventricular

volume, white matter integrity, and intellectual outcomes in spina bifida and hydrocephalus. *Journal of Neurosurgery: Pediatrics, 15*(4), 410-419.

Winklewski, P. J., Sabisz, A., Naumczyk, P., Jodzio, K., Szurowska, E., & Szarmach, A. (2018). Understanding the Physiopathology Behind Axial and Radial Diffusivity Changes-What Do We Know? *Front Neurol, 9*, 92. https://doi.org/10.3389/fneur.2018.00092

Wu, Y., Green, N. L., Wrensch, M. R., Zhao, S., & Gupta, N. (2007). Ventriculoperitoneal shunt complications in California: 1990 to 2000. *Neurosurgery, 61*(3), 557-563.

Xia, M., Wang, J., & He, Y. (2013). BrainNet Viewer: a network visualization tool for human brain connectomics. *PLoS One, 8*(7), e68910.

Yuan, W., Holland, S. K., Shimony, J. S., Altaye, M., Mangano, F. T., Limbrick, D. D., Jones, B. V., Nash, T., Rajagopal, A., Simpson, S., Ragan, D., & McKinstry, R. C. (2015). Abnormal structural connectivity in the brain networks of children with hydrocephalus. *Neuroimage Clin, 8*, 483-492. https://doi.org/10.1016/j.nicl.2015.04.015

Zalesky, A., Fornito, A., & Bullmore, E. T. (2010, Dec). Network-based statistic: identifying differences in brain networks. *Neuroimage, 53*(4), 1197-1207. https://doi.org/10.1016/j.neuroimage.2010.06.041

Zhang, F., Daducci, A., He, Y., Schiavi, S., Seguin, C., Smith, R., Yeh, C.-H., Zhao, T., & O'Donnell, L. J. (2022). Quantitative mapping of the brain's structural connectivity using diffusion MRI tractography: a review. *Neuroimage,* 118870.

Zhao, S. X., Ma, H. L., Lv, F. R., Zhang, Z. W., Chen, B., & Xiao, Y. H. (2020, Jun 19). Lateral ventricular volume and calcarine sulcus depth: a fetal MRI analysis of mild ventriculomegaly: A STROBE compliant article. *Medicine (Baltimore), 99*(25), e20679. https://doi.org/10.1097/MD.0000000000020679

Zielinska, D., Rajtar-Zembaty, A., & Starowicz-Filip, A. (2017, May - Jun). Cognitive disorders in children's hydrocephalus. *Neurol Neurochir Pol, 51*(3), 234-239. https://doi.org/10.1016/j.pjnns.2017.02.001

Appendices

Appendix A: Settings for all registration programs

SyN ANTs:

-d 3
-f *templateImage*
-m *participantImage*
-o *conditionLabel*
-t s
-r 4
-s 26
-g 0.1
-p d
-j 0
-y 0
-z 1

DARTEL Toolbox:

Segmentation Step:

- Data
  - Volumes: *participantImages*
  - Bias regularisation: no regularisation
  - Bias FWHM: No correction
  - Save Bias Corrected: Save Nothing
- Tissue
  - Tissue probability map: TPM.nii, 1
  - Num. Gaussians: 1
  - Native Tissue: Native + Dartel Imported
  - Warped Tissue: None
  - Tissue probability map: TPM.nii, 2
  - Num. Gaussians: 1
  - Native Tissue: Native + Dartel Imported
  - Warped Tissue: None
  - Tissue probability map: TPM.nii, 3
  - Num. Gaussians: 2
  - Native Tissue: Native + Dartel Imported
  - Warped Tissue: None
  - Tissue probability map: TPM.nii, 4
  - Num. Gaussians: 3
  - Native Tissue: Native + Dartel Imported
  - Warped Tissue: None
  - Tissue probability map: TPM.nii, 5
  - Num. Gaussians: 4
  - Native Tissue: Native + Dartel Imported

Warped Tissue: None
Tissue probability map: TPM.nii, 6
Num. Gaussians: 2
Native Tissue: Native + Dartel Imported
Warped Tissue: None
Warping & MRF
MRF Parameter: 1
Clean Up: Light Clean
Warping Regularisation: 1x5 double
Affine Regularisation: ICBM space template – European brains
Smoothness: 0
Sampling distance: 3
Deformation Fields: None
Run Dartel (create Template)
Images: *participantImages*
Settings
Template basename: Template
Regularisation Form: Linear Elastic Energy
Outer iterations
Inner Iterations: 3
Reg params: [4 2 1e-06]
Time Steps: 1
Smoothing Parameter: 16
Inner Iterations: 3
Reg params: [2 1 1e-06]
Time Steps: 1
Smoothing Parameter: 8
Inner Iterations: 3
Reg params: [1 0.5 1e-06]
Time Steps: 2
Smoothing Parameter: 4
Inner Iterations: 3
Reg params: [0.5 0.25 1e-06]
Time Steps: 4
Smoothing Parameter: 2
Inner Iterations: 3
Reg params: [0.25 0.125 1e-06]
Time Steps: 16
Smoothing Parameter: 1
Inner Iterations: 3
Reg params: [0.25 0.125 1e-06]
Time Steps: 64
Smoothing Parameter: 0.5
Optimisation Settings
LM Regularisation: 0.01
Cycles: 3

Iterations: 3
Normalize to MNI Space
Dartel Template: *templateImage*
Voxel sizes: [1 1 1]
Bounding box: 2x3 double
Preserve: Preserve Amount
Gaussian FWHM: [8 8 8]

DRAAMS:

-S *participantImage*
-T *templateImage*
-O *outputRegisteredImage*
-D *outputDeformationField*

FLIRT

-in *participantImage*
-ref *templateImage*
-out *outputImage*
-omat *outputMatrix*
-cost corratio
-searchcost corratio
-anglerep euler
-interp trilinear
-sincwidth 7
-bins 256
-dof 12
-searchrx -90 90 FLIRT2 uses -10 10
-searchry -90 90 FLIRT2 uses -10 10
-searchrz -90 90 FLIRT2 uses -10 10
-coarsesearch 60
-finesearch 18

FNIRT

-ref *templateImage*
-in *participantImage*
-aff *affineTransformation*
-iout *outputImage*
-fout *outputField*
-cout *outputFiledCoefficients*
-applyrefmask 1
-applyinmask 1
-imprefm 1
-impinm 1
-imprefval 0
-impinval 0
-miter 5,5,5,5
-subsamp 4,2,1,1

-warpres 10,10,10
-splineorder 3
-infwhm 6,4,2,2
-reffwhm 4,2,0,0
-regmod bending_energy
-ssqlambda 1
-jacrange 0.01, 100.0
-refderiv 0
-intorder 5
-biasres 50,50,50
-biaslambda 10000
-estint 1
-numprec double
-interp linear

Appendix B: Region to region white matter tract details.

Region 1 → Region 2	Streamline Count network#(t-statistic)		FA network#(t-statistic)		MD network#(t-statistic)		AD network#(t-statistic)		RD network#(t-statistic)	
	PH<HC	PH>HC	PH<HC	PH>HC	PH<HC	PH>HC	PH<HC	PH>HC	PH<HC	PH>HC
Amygdala_R → Calcarine_R	-	-	-	-	-	2(5.61)	-	-	-	2(5.21)
Amygdala_R → Lingual_R	-	-	-	-	-	2(6.61)	-	-	-	2(7.48)
Amygdala_R → Occipital_Sup_R.	-	-	-	-	-	2(5.28)	-	-	-	-
Amygdala_R → Temporal_Mid_R	-	-	-	-	-	2(5.80)	-	1(5.14)	-	-
Angular_R → Pallidum_R	-	-	-	-	-	-	-	1(5.15)	-	-
Calcarine_L → Putamen_L	-	-	2(4.95)	-	-	-	-	-	-	1(4.78)
Calcarine_L → Temporal_Mid_L	-	-	2(4.94)	-	-	-	-	-	-	-
Calcarine_L → Temporal_Pole_Sup_L	-	-	2(5.77)	-	-	-	-	-	-	1(4.77)
Calcarine_L → Fusiform_L	-	-	-	-	-	-	-	-	-	1(5.05)
Calcarine_L → Thalamus_L	-	-	-	-	-	1(5.03)	-	-	-	1(5.36)
Calcarine_R → Cuneus_R	-	-	-	-	-	-	-	1(4.75)	-	-
Calcarine_R → Occipital_Sup_R	-	-	-	-	-	2(6.12)	-	1(6.29)	-	-
Calcarine_R → Putamen_R	-	-	-	-	-	2(5.02)	-	-	-	-
Calcarine_R → Temporal_Sup_R	-	-	-	-	-	2(5.12)	-	-	-	2(4.79)
Caudate_R → Thalamus_R	-	-	-	-	-	2(4.79)	-	1(5.40)	-	-
Cerebelum_3_R → Cerebelum_4_5_R	-	2(5.48)	-	-	-	-	-	-	-	-
Cerebelum_4_5_L → Vermis_6	-	2(4.11)	-	-	-	-	-	-	-	-

Cerebelum_4_5_R → Cerebelum_6_R	-	2(4.37)	-	-	-	-	-	-	-	-
Cerebelum_4_5_R → Vermis_3	-	2(5.03)	-	-	-	-	-	-	-	-
Cerebelum_4_5_R → Vermis_6	-	2(4.46)	-	-	-	-	-	-	-	-
Cerebelum_6_R → Vermis_6	-	2(4.62)	-	-	-	-	-	-	-	-
Cerebelum_6_R → Vermis_7	-	2(5.39)	-	-	-	-	-	-	-	-
Cerebelum_6_R → Vermis_8	-	2(4.97)	-	-	-	-	-	-	-	-
Cerebelum_Crus2_L → Vermis_7	-	2(3.73)	-	-	-	-	-	-	-	-
Cerebelum_Crus2_R → Cerebelum_6_R	-	2(5.08)	-	-	-	-	-	-	-	-
Cingulum_Mid_R → Caudate_R	-	-	-	-	-	-	-	1(4.91)	-	-
Cingulum_Post_L → Cuneus_L	1(3.70)	-	-	-	-	-	-	-	-	-
Cuneus_L → Occipital_Mid_L	-	-	-	-	-	-	-	-	-	1(4.84)
Cuneus_L → Thalamus_L	-	-	-	-	-	1(4.09)	-	-	-	1(5.22)
Cuneus_R → Fusiform_R	-	-	-	-	-	2(7.24)	-	-	-	2(7.23)
Cuneus_R → Lingual_R	-	-	-	-	-	2(5.86)	-	1(4.96)	-	2(4.87)
Cuneus_R → Pallidum_R	-	-	-	-	-	2(5.04)	-	-	-	-
Frontal_Inf_Orb_L → Temporal_Pole_Mid_L	-	-	-	-	-	-	-	-	1(4.87)	-
Frontal_Mid_R → Insula_R	-	1(5.48)	-	-	-	-	-	-	-	-
Frontal_Sup_L → Caudate_L	-	-	-	1(5.30)	-	-	-	-	-	-
Frontal_Sup_Medial_L → Caudate_L	-	-	-	1(5.03)	-	-	-	-	-	-
Frontal_Sup_Medial_L → Insula_L	-	-	-	1(5.97)	-	-	-	-	-	-

Frontal_Sup_Medial_L → Pallidum_L	-	-	-	1(5.44)	-	-	-	-	-	-
Frontal_Sup_Medial_L → Putamen_L	-	-	-	1(5.75)	-	-	-	-	-	-
Frontal_Sup_Orb_L → Temporal_Pole_Mid_L	-	-	-	-	1(4.73)	-	-	-	1(4.76)	-
Frontal_Sup_R → Putamen_R	-	-	-	2(4.79)	-	-	-	-	-	-
Fusiform_L → Temporal_Pole_Sup_L	-	-	-	-	-	-	-	-	-	1(4.72)
Fusiform_R → Putamen_R	-	-	-	-	-	2(4.64)	-	-	-	-
Hippocampus_L → Cuneus_L	1(3.99)	-	-	-	-	1(5.14)	-	-	-	1(5.06)
Hippocampus_L → Hippocampus_R	1(3.75)	-	-	-	-	-	-	-	-	-
Hippocampus_L → Lingual_L	-	-	-	-	-	1(5.38)	-	-	-	1(5.66)
Hippocampus_L → Occipital_Sup_L	-	-	-	-	-	1(5.02)	-	-	-	1(5.03)
Hippocampus_L → ParaHippocampal_L	-	-	-	-	-	1(6.56)	-	-	-	1(6.01)
Hippocampus_L → Precuneus_L	-	-	-	-	-	-	-	2(5.11)	-	-
Hippocampus_R → Lingual_L	-	-	1(4.91)	-	-	-	-	-	-	-
Hippocampus_R → Lingual_R	-	-	1(5.65)	-	-	2(7.53)	-	-	-	2(9.72)
Hippocampus_R → Precuneus_R	-	-	1(6.00)	-	-	2(7.58)	-	-	-	2(8.37)
Hippocampus_R → Angular_R	-	-	-	-	-	-	-	1(5.00)	-	-
Hippocampus_R → Calcarine_R	-	-	-	-	-	-	-	-	-	2(4.72)

Hippocampus_R → Cuneus_R	-	-	-	-	-	2(5.34)	-	1(5.48)	-	-
Hippocampus_R → Occipital_Inf_R	-	-	-	-	-	2(4.93)	-	-	-	-
Hippocampus_R → Occipital_Mid_R	-	-	-	-	-	2(6.54)	-	1(7.39)	-	2(4.90)
Hippocampus_R → Occipital_Sup_R	-	-	-	-	-	2(5.66)	-	1(6.87)	-	-
Hippocampus_R → Precuneus_L	1(4.20)	-	-	-	-	-	-	-	-	-
Hippocampus_R → Temporal_Mid_R	-	1(4.37)	-	-	-	-	-	-	-	-
Hippocampus_R → Thalamus_L	1(3.78)	-	-	-	-	-	-	-	-	-
Insula_L → Lingual_L	-	-	-	-	-	1(4.98)	-	-	-	1(5.61)
Insula_R → Calcarine_R	-	-	-	-	-	2(4.86)	-	-	-	-
Insula_R → Occipital_Mid_R	-	-	-	-	-	2(5.29)	-	1(4.90)	-	-
Insula_R → Parietal_Inf_R	-	-	-	-	-	-	-	1(4.86)	-	-
Insula_R → Precuneus_R	-	-	-	-	-	-	-	1(4.81)	-	-
Insula_R → Temporal_Mid_R	-	1(5.08)	-	-	-	-	-	-	-	-
Lingual_L → Precuneus_R	-	-	1(5.73)	-	-	-	-	-	-	-
Lingual_L → Thalamus_L	-	-	1(4.99)	-	-	-	-	-	-	1(5.82)
Lingual_L → Fusiform_L	-	-	-	-	-	-	-	2(4.89)	-	-
Lingual_L → Precuneus_L	-	-	-	-	-	1(5.52)	-	-	-	1(5.80)
Lingual_L → Putamen_L	-	-	-	-	-	-	-	-	-	1(4.98)
Lingual_L → Temporal_Sup_L	-	-	-	-	-	-	-	-	-	1(4.77)

Lingual_R → Cerebelum_3_R	--	-	1(4.92)	-	-	-	-	-	-	-
Lingual_R → Vermis_6	--	-	-	3(6.42)	-	2(5.89)	-	1(6.30)	-	2(5.58)
Lingual_R → Cerebelum_6_R	-	-	-	-	-	-	-	1(4.84)	-	-
Lingual_R → Fusiform_R	-	-	-	-	-	2(4.79)	-	-	-	-
Lingual_R → Occipital_Sup_R	-	-	-	-	-	2(6.02)	-	-	-	2(4.99)
Lingual_R → Parietal_Sup_R	-	-	-	-	-	2(5.03)	-	-	-	-
Lingual_R → Precuneus_R	-	-	-	-	-	-	-	-	-	2(5.17)
Lingual_R → Putamen_R	-	-	-	-	-	-	-	-	-	2(5.73)
Lingual_R → Temporal_Inf_R	-	-	-	-	-	2(4.93)	-	-	-	2(5.25)
Lingual_R → Temporal_Mid_R	-	-	-	-	-	2(5.92)	-	-	-	2(6.10)
Lingual_R → Temporal_Pole_Mid_R	2(4.60)	-	-	-	-	2(5.78)	-	-	-	2(6.45)
Lingual_R → Temporal_Sup_R	-	-	-	-	-	2(4.84)	-	-	-	2(4.75)
Lingual_R → Thalamus_R	-	-	-	-	-	-	-	-	-	2(5.10)
Occipital_Inf_L → Thalamus_L	-	-	1(5.29)	-	-	-	-	-	-	-
Occipital_Inf_R → Putamen_R	-	-	-	-	-	2(5.07)	-	-	-	2(4.79)
Occipital_Mid_R → Pallidum_R	-	-	-	-	-	2(6.15)	-	1(5.20)	-	-
Occipital_Mid_R → Precuneus_R	-	-	-	-	-	-	-	1(5.01)	-	-
Occipital_Mid_R → Putamen_R	-	-	-	-	-	2(5.76)	-	1(5.23)	-	-
Occipital_Mid_R → Temporal_Pole_Mid_R	-	-	-	-	-	2(4.77)	-	1(4.80)	-	-

Occipital_Mid_R → Thalamus_R	-	-	-	-	-	2(5.36)	-	1(5.10)	-	2(4.74)
Occipital_Sup_L → Thalamus_L	1(4.64)	-	-	-	-	-	-	-	-	1(4.97)
Occipital_Sup_R → Pallidum_R	-	-	-	-	-	2(5.07)	-	-	-	-
Pallidum_R → Temporal_Mid_R	-	-	-	-	-	2(6.14)	-	1(5.28)	-	2(4.92)
Paracentral_Lobule_L → Thalamus_L	1(4.82)	-	-	-	-	-	-	-	-	-
ParaHippocampal_L → Calcarine_L	-	-	-	-	-	1(5.17)	-	-	-	1(5.49)
ParaHippocampal_L → Cuneus_L	-	-	-	-	-	-	-	2(5.58)	-	-
ParaHippocampal_L → Fusiform_L	-	-	-	-	-	1(5.07)	-	-	-	1(5.18)
ParaHippocampal_L → Lingual_L	-	-	-	-	-	1(5.43)	-	2(5.81)	-	1(5.00)
ParaHippocampal_L → Occipital_Sup_L	-	-	-	-	-	1(4.74)	-	2(4.88)	-	-
ParaHippocampal_L → Parietal_Sup_L	-	-	-	-	-	-	-	2(4.91)	-	-
ParaHippocampal_L → Precuneus_L	-	-	-	-	-	-	-	2(5.26)	-	-
ParaHippocampal_R → Occipital_Sup_R	-	-	-	-	-	2(5.16)	-	-	-	-
ParaHippocampal_R → Calcarine_R	-	-	-	-	-	2(5.41)	-	-	-	2(6.13)
ParaHippocampal_R → Cuneus_R	-	-	-	-	-	2(5.15)	-	1(4.76)	-	-
ParaHippocampal_R → Lingual_R	-	-	-	-	-	2(5.13)	-	-	-	-

ParaHippocampal_R → Precuneus_R	-	-	-	-	-	2(5.68)	-	-	-	2(6.13)
Parietal_Inf_L → Caudate_L	-	-	-	-	-	-	-	2(5.28)	-	-
Parietal_Inf_R → Pallidum_R	-	-	-	-	-	-	-	1(4.82)	-	-
Parietal_Inf_R → Thalamus_R	-	-	-	-	-	-	-	1(5.18)	-	-
Parietal_Sup_L → Caudate_L	-	-	-	-	-	-	-	2(5.00)	-	-
Parietal_Sup_L → Heschl_L	-	-	-	-	-	-	-	2(4.82)	-	-
Parietal_Sup_R → Heschl_R	-	-	-	-	-	-	-	1(5.53)	-	-
Precentral_L → Caudate_L	-	-	-	1(5.51)	-	-	-	-	-	-
Precentral_R → Caudate_R	-	-	-	-	-	-	-	1(5.07)	-	-
Precentral_R → Thalamus_R	-	-	-	-	-	-	-	1(4.90)	-	-
Precuneus_L → Caudate_L	-	-	-	-	-	-	-	2(5.18)	-	-
Precuneus_L → Thalamus_L	-	-	-	-	-	1(5.07)	-	2(7.07)	-	-
Precuneus_R → Pallidum_R	-	-	-	-	-	-	-	1(6.32)	-	-
Precuneus_R → Putamen_R	-	-	-	-	-	-	-	1(5.53)	-	-
Precuneus_R → Temporal_Mid_R	-	-	-	-	-	-	-	1(5.09)	-	-
Precuneus_R → Temporal_Sup_R	-	-	-	-	-	-	-	1(6.41)	-	-
Putamen_R → Temporal_Inf_R	-	-	-	-	-	-	-	1(5.19)	-	-
Putamen_R → Temporal_Mid_R	-	-	-	-	-	2(5.49)	-	1(5.67)	-	-
Putamen_R → Temporal_Sup_R	-	-	-	-	-	-	-	1(5.41)	-	-
Supp_Motor_Area_R → Caudate_R	-	-	-	-	-	-	-	1(5.66)	-	-
Supp_Motor_Area_R → Cerebelum_3_R	-	-	-	-	-	-	-	1(5.50)	-	-

SupraMarginal_R → Heschl_R	-	-	-	-	-	-	-	1(5.32)	-	-
SupraMarginal_R → Pallidum_R	-	-	-	-	-	-	-	1(5.30)	-	-
SupraMarginal_R → Putamen_R	-	-	-	-	-	-	-	1(5.08)	-	-
SupraMarginal_R → Thalamus_R	-	-	-	-	-	-	-	1(5.02)	-	-
Temporal_Mid_R → Temporal_Pole_Mid_R	2(3.87)	-	-	-	-	-	-	-	-	-
Thalamus_L → Thalamus_R	-	-	1(5.51)	-	-	-	-	-	-	
Thalamus_L → Cerebelum_4_5_L	-	-	-	-	-	1(4.92)	-	2(4.95)	-	-
Thalamus_R → Vermis_3		-	-	-	-	2(5.46)	-	1(4.73)	-	2(5.67)
Vermis_1_2 → Vermis_10	-	2(4.20)	-	-	-	-	-	-	-	-
Vermis_3 → Vermis_4_5	-	2(4.83)	-	-	-	-	-	-	-	-
Vermis_4_5 → Vermis_10	-	2(3.84)	-	-	-	-	-	-	-	-
Vermis_6 → Vermis_10	-	2(5.99)	-	-	-	-	-	-	-	-
Vermis_6 → Vermis_10	-	2(4.44)	-	-	-	-	-	-	-	-
Vermis_6 → Vermis_7	-	2(5.43)	-	-	-	-	-	-	-	-
Vermis_6 → Vermis_8	-	2(4.74)	-	-	-	-	-	-	-	-

Curriculum Vitae

Name:	Renee-Marie Ragguett
Post-secondary Education and Degrees:	University of Toronto Toronto, Ontario, Canada 2011-2016 H.BSc
	The University of Western Ontario London, Ontario, Canada 2017-2020 H.BSc
	The University of Western Ontario London, Ontario, Canada 2020-2022 M.ESc
Honours and Awards:	Natural Sciences and Engineering Research Council (NSERC-USRA) 2020
	Natural Sciences and Engineering Research Council (NSERC- CGS-M) 2021-2022

Publications:

Conference Presentations:

Ragguett, R. M., Eagleson, R., de Ribaupierre, S. (Feb, 2021). Assessing Ventricle Volume and Periventricular Functional Connectivity in Shunt Treated Pediatric Onset Hydrocephalus. *Neuroscience Research Day*. Online.

Ragguett, R. M., Eagleson, R., de Ribaupierre, S. (Oct, 2021). Assessing Ventricle Volume and Periventricular Functional Connectivity in Shunt Treated Pediatric Onset Hydrocephalus. *Basic and Clinical Multimodal Imaging*. Online.

Ragguett, R. M., Eagleson, R., de Ribaupierre, S. (May, 2022). Whole-Brain Tractography in Shunt-Treated Pediatric Hydrocephalus and the Impact of Postoperative Ventricle Volume. *Child Health Research Day*. London, Ontario.

Ragguett, R. M., Eagleson, R., de Ribaupierre, S. (May, 2022). Postoperative Ventricle Volume and Whole-Brain Tractography in Pediatric Hydrocephalus. *CNS Research Day*. London, Ontario.

Ragguett, R. M., Eagleson, R., de Ribaupierre, S. (June, 2022). Normalization of Pathological Brains: Insights from Shunt-Treated Pediatric Hydrocephalus. *Organization for Human Brain Mapping*. Abstract accepted. Online/Glasgow, Scotland.

Ragguett, R. M., Eagleson, R., de Ribaupierre, S. (July, 2022). Network Characterization of the Prefrontal Cortex in Children with Intractable Epilepsy. *European Epilepsy Congress*. Abstract accepted. Geneva, Switzerland.